

# Solar zenith angle dependence of relationships between energy inputs to the ionosphere and ion outflow fluxes

Naritoshi Kitamura (✉ [kitamura@eps.s.u-tokyo.ac.jp](mailto:kitamura@eps.s.u-tokyo.ac.jp))

The University of Tokyo <https://orcid.org/0000-0002-2397-273X>

Kanako Seki

The University of Tokyo

Kunihiro Keika

The University of Tokyo

Yukitoshi Nishimura

Boston University

Tomoaki Hori

Nagoya University

Masafumi Hirahara

Nagoya University

Eric J Lund

University of New Hampshire Institute for the Study of Earth Oceans and Space

Lynn M Kistler

University of New Hampshire Institute for the Study of Earth Oceans and Space

Robert J Strangeway

University of California Los Angeles

---

## Full paper

**Keywords:** Auroral ion outflow, polar ionosphere, auroral precipitation, FAST satellite, cleft ion fountain, ion conics, ion beams

**Posted Date:** April 5th, 2021

**DOI:** <https://doi.org/10.21203/rs.3.rs-388101/v1>

**License:**   This work is licensed under a Creative Commons Attribution 4.0 International License.

[Read Full License](#)

---

1 **Title page:**

2 **Title: Solar zenith angle dependence of relationships between energy inputs to the**  
3 **ionosphere and ion outflow fluxes**

4 Author #1: Naritoshi Kitamura, Department of Earth and Planetary Science, Graduate  
5 School of Science, The University of Tokyo, Japan, kitamura@eps.s.u-tokyo.ac.jp

6 Author #2: Kanako Seki, Department of Earth and Planetary Science, Graduate School  
7 of Science, The University of Tokyo, Japan, k.seki@eps.s.u-tokyo.ac.jp

8 Author #3: Kunihiro Keika, Department of Earth and Planetary Science, Graduate  
9 School of Science, The University of Tokyo, Japan, keika@eps.s.u-tokyo.ac.jp

10 Author #4: Yukitoshi Nishimura, Department of Electrical and Computer Engineering  
11 and Center for Space Physics, Boston University, Boston, MA, USA, toshi16@bu.edu

12 Author #5: Tomoaki Hori, Institute for Space-Earth Environmental Research, Nagoya  
13 University, Furo-cho, Chikusa-ku, Nagoya, Japan, tomo.hori@nagoya-u.jp

14 Author #6: Masafumi Hirahara, Institute for Space-Earth Environmental Research,  
15 Nagoya University, Furo-cho, Chikusa-ku, Nagoya, Japan, hirahara@nagoya-u.jp

16 Author #7: Eric J. Lund, Institute for the Study of Earth, Oceans, and Space, Institute

17 for the Study of Earth, Oceans, and Space, University of New Hampshire, Durham, NH,

18 USA; College Brook Scientific, Durham, NH, USA, eric.lund@unh.edu

19 Author #8: Lynn M. Kistler, Institute for the Study of Earth, Oceans, and Space,

20 University of New Hampshire, Durham, NH, USA; Department of Physics, University

21 of New Hampshire, Durham, NH, USA, lynn.kistler@unh.edu

22 Author #9: Robert J. Strangeway, Department of Earth, Planetary, and Space Sciences,

23 University of California in LA, Los Angeles, CA, USA, strange@igpp.ucla.edu

24 **Corresponding author: Naritoshi Kitamura**

25

## 26 **Abstract**

27 The ionosphere is one of the important sources for magnetospheric plasma, particularly  
28 for heavy ions with low charge states. We investigate the effect of solar illumination on  
29 the number flux of ion outflow using data obtained by the Fast Auroral Snapshot  
30 satellite at 3000–4150 km altitude from 7 January 1998 to 5 February 1999. We derive  
31 empirical formulas between energy inputs and outflowing ion number fluxes for various  
32 solar zenith angle ranges. We found that the outflowing ion number flux under sunlit  
33 conditions increases more steeply with increasing electron density in the loss cone or  
34 with increasing precipitating electron density ( $>50$  eV), compared with the ion flux  
35 under dark conditions. Under ionospheric dark conditions, weak electron precipitation  
36 can drive ion outflow with small averaged fluxes ( $\sim 10^7$  cm<sup>-2</sup> s<sup>-1</sup>). The slopes of  
37 relations between the DC and Alfvén Poynting fluxes and outflowing ion number fluxes  
38 show no clear dependence on solar zenith angle. Intense ion outflow events ( $>10^8$  cm<sup>-2</sup>  
39 s<sup>-1</sup>) occur mostly under sunlit conditions (solar zenith angle  $< 90^\circ$ ). Thus, it is  
40 presumably difficult to drive intense ion outflows under dark conditions, because of a  
41 lack of the solar illumination (low ionospheric density and/or small scale height owing

42 to low plasma temperature).

43

## 44 **Keywords**

45 Auroral ion outflow, polar ionosphere, auroral precipitation, FAST satellite, cleft ion

46 fountain, ion conics, ion beams

47

## 48 **Main Text**

### 49 **1. Introduction**

50 Quantifying the properties of outflowing ionospheric ions is one of the most

51 important subjects for magnetospheric studies, because the physical characteristics of

52 the magnetosphere are modulated significantly by outflowing ions. Many satellite

53 observations have demonstrated that ionospheric  $O^+$  ions are supplied to the plasma

54 sheet and inner magnetosphere, especially during geomagnetically active periods (e.g.,

55 Daglis 1997; Yao et al. 2008a; Ebihara et al. 2009; Mouikis et al. 2010; Ohtani et al.

56 2011; Kronberg et al. 2012, 2015; Maggiolo and Kistler 2014; Kistler and Mouikis

57 2016; Keika et al. 2018a, 2018b; Mitani et al., 2019; Mouikis et al., 2019; Kistler et al.

58 2019). Various modeling and observational studies have suggested that an increase in  
59 the ionospheric  $O^+$  ions in the magnetosphere would affect reconnection processes (e.g.,  
60 Shay and Swisdak 2004; Karimabadi et al. 2011; Liu et al. 2015; Fuselier et al., 2019;  
61 Tenfjord et al., 2019), location of the tail reconnection (Brambles et al. 2010; Garcia et  
62 al. 2010; Wiltberger et al. 2010; Yu and Ridley 2013), growth and propagation of  
63 electromagnetic ion cyclotron waves (e.g., Omidi et al. 2013; Denton et al. 2014; Nosé  
64 et al., 2020), and development and decay of the ring current (e.g., Hamilton et al. 1988;  
65 Keika et al. 2006; Glocer et al. 2009a, 2009b, 2013; Welling et al. 2011; Ilie et al. 2015;  
66 Menz et al. 2019). Moreover, modeling studies by Brambles et al. (2011, 2013),  
67 Ouellette et al. (2013), Varney et al. (2016), and Zhang et al. (2020) showed that  
68 inclusion of  $O^+$  ion outflows can change the mode of global magnetospheric convection:  
69 from steady convection to sawtooth oscillations. Observations and effects of  $O^+$  ions in  
70 the magnetosphere are summarized in more detail in review papers by Keika et al.  
71 (2013), Kronberg et al. (2014), Welling et al. (2016), and Yamauchi (2019).

72 Some of the  $O^+$  ions are lost to the interplanetary space through the boundary layer  
73 (Zong et al. 2004; Bouhram et al. 2005; Cohen et al. 2016; Zeng et al. 2020), plasma

74 mantle (Slapak et al. 2017; Schillings et al. 2019, 2020), and/or distant tail (Seki et al.  
75 1998; Kistler et al. 2010). Additionally, some O<sup>+</sup> ions are lost as energetic neutral atoms  
76 due to the charge exchange process (Keika et al. 2006; Valek et al. 2018). Thus, the  
77 understanding of ion outflow from the ionosphere also contributes to the understanding  
78 of atmospheric loss from magnetized planets.

79 To include ion outflows from the ionosphere in global magnetospheric simulations,  
80 moments of the outflowing ion distribution function can be used as the boundary  
81 conditions at the inner boundary, which is typically located at ~2.5 Earth radii ( $R_E$ ) in  
82 geocentric distance. If temporal variations of the ion outflows are important for the  
83 studies, time-dependent inner boundary conditions are necessary. There have been two  
84 approaches for it: one is to use ion outflows from ionospheric simulations (e.g., Schunk  
85 and Sojka 1997; Barakat and Schunk 2006; Glozer et al. 2012, 2018, 2020; Pham et al.  
86 2021; Varney et al. 2015, 2016; Welling et al. 2015, 2016), and the other is to use  
87 empirical relations between energy inputs and ion outflow fluxes (Fok et al. 2006, 2011;  
88 Moore et al. 2007, 2010; Brambles et al. 2010, 2011, 2013; Damiano et al. 2010;  
89 Perroomian et al. 2011; Ouellette et al. 2013). The present study provides such empirical

90 relations that include effects of the solar illumination. Such empirical relations may also  
91 be useful for rough validation of ion outflow simulations.

92     Using data obtained by the Fast Auroral SnapshoT (FAST) satellite, statistical studies  
93 by Strangeway et al. (2005) and Brambles et al. (2011) indicated that fluxes of ion  
94 outflows are correlated well with the precipitating electron density ( $>50$  eV), electron  
95 density in the loss cone ( $>50$  eV), and DC and Alfvén Poynting fluxes. They derived  
96 empirical formulas between these energy inputs to the ionosphere and outflowing ion  
97 number fluxes at  $\sim 4000$  km altitude using the data obtained near the cusp region in the  
98 dayside (mostly in the postnoon sector) during a geomagnetic storm (24–26 September  
99 1998, which included  $\sim 30$  orbit passes). Zheng et al. (2005) also derived similar  
100 empirical formulas using data obtained by the Polar spacecraft at  $\sim 5000$  km altitude (37  
101 events, mostly in the dayside). Recently, Zhao et al. (2020) updated the empirical  
102 formulas derived by Strangeway et al. (2005) and Brambles et al. (2011) using the mass  
103 resolved ion data derived by the FAST satellite during the same geomagnetic storm as  
104 previously studied by them. Hatch et al. (2020a) focused on the east-west magnetic field  
105 fluctuations, and investigated the relation between the magnetic field fluctuations and

106 ion outflows around the cusp for four geomagnetic storms in various seasons. They  
107 examined the correlation of the ion outflow flux with magnetic fluctuations and showed  
108 that the outflow flux has a smaller increase rate with increasing amplitude of the east-  
109 west fluctuations in winter than in summer and equinox seasons.

110 The solar illumination (or season) strongly affects the ionosphere in terms of the  
111 condition under which the ionosphere receives energy inputs from the magnetosphere  
112 (Garner et al. 2010; Hatch et al. 2020b; Zhang et al. 2010). A statistical study by  
113 Kitamura et al. (2011) that used data from the Akebono and Intercosmos satellites, and  
114 the European incoherent scatter Svalbard radar reported that the temperature and scale  
115 height of background thermal plasma in the topside ionosphere are strongly controlled  
116 by the solar zenith angle (SZA). It causes large seasonal dependence of the electron  
117 density around 2000 km altitude in the polar region under quiet geomagnetic conditions  
118 (Kitamura et al. 2009). Using data obtained by the Defense Meteorological Satellite  
119 Program, Ma et al. (2018) investigated the effect of solar illumination on ion upflows  
120 and found that the effect is not simple. For example, they showed that high speed  
121 upflow can occur under dark conditions, while upflows with large density can occur

122 under sunlit conditions. Some statistical studies using incoherent scatter radar data have  
123 identified seasonal variation of the occurrence frequency of ion upflows (Foster et al.  
124 1998; Liu et al. 2001; Buchert et al. 2004; Ji et al. 2019; Ren et al. 2020), although the  
125 seasonal variation seems to depend on the observed altitude and/or location of the radar.  
126 The occurrence of upward ion beams is also strongly affected by the solar illumination;  
127 the occurrence rate is lower under sunlit ionospheric conditions (on the basis of  
128 measurements below ~4000 km altitude) (Cattell et al. 2013), and is also lower in  
129 winter, which mostly corresponds to dark conditions (on the basis of measurements  
130 around ~6000 km altitude) (Collin et al. 1998). The occurrence frequency of ion conics  
131 (or transversely accelerated ions) at ~1500 km altitude is higher in winter, which period  
132 corresponds mostly to dark conditions (Klumpar 1979; Norqvist et al. 1998). Broadband  
133 extremely low-frequency waves (observed below ~10,000 km altitude (Kasahara et al.  
134 2001)) and electromagnetic ion cyclotron waves (500–4000 km (Saito et al. 1987) and  
135 ~1500 km altitude (Erlandson and Zanneti 1998; Hamrin et al. 2002)), which are  
136 thought to be the main driving processes of ion conics, also tend to be preferentially  
137 generated under winter and/or dark conditions. These various types of observations

138 support the importance of solar illumination (ionospheric conditions) for ion outflows.

139 Thus, the solar illumination may affect the empirical relationships between the energy

140 inputs and outflowing ion number fluxes. Since the SZA at the magnetic footprint of the

141 events used by Strangeway et al. (2005) and Brambles et al. (2011) was smaller than

142  $92^\circ$ , their empirical formulas represent those under sunlit ionospheric conditions.

143 Some modeling studies of ion outflows have shown a seasonal dependence (Demars

144 and Schunk 2001, 2002) or interhemispheric asymmetry (Barakat et al. 2015; Glocer et

145 al. 2020) of ion outflows, although the models are incomplete because physical

146 processes of ion outflows have not been fully understood yet.

147 To understand how strongly (sunlit or dark) ionospheric conditions affect ion

148 outflows, we derive empirical formulas of outflowing ion number fluxes as a function

149 of each energy input (electron density in the loss cone ( $>50$  eV), precipitating electron

150 density ( $>50$  eV), DC and Alfvén Poynting fluxes) for a wide SZA range ( $45^\circ$ – $145^\circ$ ),

151 using data obtained by the FAST satellite (3000–4150 km altitude). The structure of this

152 manuscript goes in the following way: Section 2 describes the datasets and the event

153 selection criteria we used. Sections 3 and 4 present the results of our data analysis,

154 followed by some discussions in Section 5.

155

## 156 **2. Dataset and Selection of Ion Outflow Events**

157 The FAST satellite was launched in 1996 with an initial perigee, apogee, and  
158 inclination of 350 km, 4175 km, and  $83^\circ$ , respectively. The satellite was spin-stabilized  
159 with a spin period of  $\sim 5$  s. The spin axis was nearly normal to the orbital plane (Carlson  
160 et al. 1998). We used data obtained in four intervals between 7 January 1998 and 5  
161 February 1999 (7 January 1998–4 April 1998 (North), 3 May 1998–20 July 1998  
162 (South), 31 July 1998–26 October 1998 (North), and 15 December 1998–6 February  
163 1999 (South)). These periods are suitable for studying the impact of SZA, because the  
164 orbital plane of the FAST satellite tended to be aligned to the noon-midnight meridian  
165 when the apogee stayed near the pole. This orbit configuration enables the satellite to  
166 traverse the auroral zone (or cusp) at various SZAs even in a single day, owing to the  
167 shift of the magnetic pole from the rotational axis. In contrast, the satellite can only  
168 measure very limited specific SZA repeatedly in cases where the orbital plane was  
169 closely aligned to the dawn-dusk meridian. The monthly mean F10.7 index ranged

170 between 93.4 and 150.1, which is almost the same level as the solar maximum of Solar  
171 cycle 24.

172 The electron and ion spectrometers (EESA and IESA) measured two-dimensional  
173 ( $360^\circ$ ) electron and ion velocity distributions with an angular resolution of  $11.25^\circ$  (32  
174 bins) or  $5.625^\circ$  (64 bins in limited periods of IESA) in an energy range of  $\sim 4$  eV–32  
175 keV and  $\sim 3$  eV–24 keV, respectively (Carlson et al. 2001). During the data periods for  
176 the present study, the EESA and IESA covered the energy ranges with 48 energy steps.  
177 The electron density in the loss cone (see Section 4.2 for the definition) and the  
178 precipitating electron density, which was proposed by Strangeway et al. (2005) and was  
179 calculated using the energy flux and the number flux (see Section 4.3 for the definition),  
180 include electrons in the energy range of 50 eV–32 keV. This low energy limit (50 eV) is  
181 set to avoid the contamination of ionospheric photoelectrons, following Strangeway et  
182 al. (2005). Background counts were subtracted from the IESA data using count rates in  
183 the source cone (Appendix A1).

184 The low energy limit for calculations of field-aligned (upward positive) ion number  
185 fluxes was set to 10 eV to reduce the influence of small changes in spacecraft potential

186 and the effect of spacecraft motion (ram effect) on the calculation of ion number flux. In  
187 cases where the orbital velocity of FAST was not perpendicular to the magnetic field,  
188 sometimes artificial fluxes owing to the ram effect became significant below  $\sim 10$  eV;  
189 the spacecraft velocity of  $\sim 6.2$  km s<sup>-1</sup> ( $\sim 3000$  km altitude) corresponds to the energy of  
190  $\sim 3.2$  eV for O<sup>+</sup> ions. Note that this lower limit (10 eV) is higher than that used by  
191 Strangeway et al. (2005) (4 eV). This change is done to find a much larger number of  
192 events quantitatively (not with visual inspection) from times when the apogee is at  
193 various latitudes.

194 The magnetic field (Elphic et al. 2001) and electric field (Ergun et al. 2001) data were  
195 used to derive Poynting fluxes. Poynting fluxes were calculated using electric fields  
196 along the orbital velocity vector ( $E_{\text{along}_v}$ ) of the satellite (1 s average) and deviations  
197 from the International Geomagnetic Reference Field 11th generation (IGRF-11) model  
198 magnetic field (Finlay et al. 2010) perpendicular to the orbital velocity vector ( $\delta B_{\text{perp}_v}$ )  
199 (1 s average). The Poynting flux of DC fields (DC Poynting flux:  $< 0.125$  Hz) was  
200 calculated as the vector product of running averaged values of  $E_{\text{along}_v}$  and  $\delta B_{\text{perp}_v}$   
201 (window size: 7 data points) (Strangeway et al. 2005), and the Poynting flux of Alfvénic

202 waves (Alfvén Poynting flux: 0.125–0.5 Hz) was the vector product of residuals of  
203  $E_{\text{along}_V}$  and  $\delta B_{\text{perp}_V}$  after subtraction of the running averaged values (Brambles et al.  
204 2011). For these Poynting fluxes, a positive value corresponds to a downward Poynting  
205 flux. Note that the electric field perpendicular to the velocity vector of the satellite is not  
206 derived owing to lack of reliable measurements of the electric field along the spin axis.  
207 Thus, the magnitude of the Poynting fluxes is underestimated, and this incomplete  
208 Poynting flux measurement probably contributes to somewhat large scatter in some  
209 results of the present analysis on the relationship between the Poynting fluxes and the  
210 ion flux (Sections 4.4 and 4.5).

211 Ion number fluxes, electron energy and number fluxes, and Poynting fluxes were  
212 mapped to 1000 km altitude, assuming the dipole magnetic field. The particle, magnetic  
213 field, and Poynting flux data were averaged over 5 s intervals ( $\sim 1$  spin) after removing  
214 erroneous data (Appendix A2), resulting in the dataset with a uniform time resolution of  
215 5 s.

216 At magnetic footprints of the cusp, the boundary layer, and the plasma sheet, high  
217 energy ions from the magnetosphere or the solar wind precipitate into the ionosphere.

218 Since these populations contribute negatively to the ion number flux, such contribution  
219 must be separated from that of the outflowing ions. In the present study, the contribution  
220 of the precipitating ions was separated by referring to their energy difference: the energy  
221 of outflowing ions is lower than that of the precipitating ions. Practically, the upper  
222 energy limit that maximizes the field-aligned (upward positive) ion number flux (IESA)  
223 was selected from about 18, 30, 50, 100, 200, 350, 600, 1000, 2000, 4000, or 10,000 eV  
224 (per 3 or 4 energy bin, except for 4–10 keV that includes 5 energy bins) in each 5 s  
225 interval. The observed flux was then integrated up to the selected upper energy limit to  
226 evaluate a number flux of outflowing ions. Figure 1 shows an example of the data  
227 during the main phase of a geomagnetic storm ( $K_p = 4$ ,  $AL = -500$ – $-1000$  nT).

228 Electrons and high-energy (above the white line) ions from the cusp/cleft and plasma  
229 sheet were detected at  $\sim 19:42$  UT and after  $\sim 20:10$  UT, respectively. A white polygonal  
230 line in Figure 1b is the upper energy limit selected as described above. In the region  
231 where the outflowing low-energy ion number flux (Figure 1c) is large ( $>10^7$  cm $^{-2}$  s $^{-1}$ ),  
232 the precipitating ions with high energies are appropriately separated from the  
233 outflowing low-energy component.

234 Before identification of ion outflow events, intervals of significant negative  
235 spacecraft charging, which causes artificially large ion number fluxes, were identified,  
236 and were treated as data gaps. Although such negative spacecraft charging was rare  
237 around the apogee, even a small number of such events can affect the present statistical  
238 study, because real events with very large ion number flux were also rare. A more  
239 detailed explanation about the intervals is described in Appendix A3.

240 We focused on full auroral zone (or cusp) crossings as much as possible. Thus, the  
241 data obtained during orbit passes that included observations of the polar cap longer than  
242 200 s (40 data points) were used for the present statistical study. The polar cap was  
243 defined with the threshold of a mean differential energy flux ( $<10^{4.6}$  eV cm<sup>-2</sup> s<sup>-1</sup> sr<sup>-1</sup>  
244 eV<sup>-1</sup>) of the 5 s averaged low-energy ion data (110 eV–24 keV). The threshold of  
245 differential energy flux is identical to that used by Andersson et al. (2004). A more  
246 detailed explanation about the selection of the polar cap is described in Appendix A4. A  
247 green bar above the top of Figure 1 is an example of the identified polar cap periods.  
248 The orbit passes at high latitudes ( $>45^\circ$  in invariant latitude (ILAT)) were divided into  
249 an inbound and an outbound part.

250 As the candidates of the outflow region, continuous ( $\geq 10$  s,  $\geq 2$  data points) data  
251 points with mapped ion number flux larger than  $10^7$  cm<sup>-2</sup> s<sup>-1</sup> were selected. Blue bars at  
252 the top of Figure 1 are an example of the candidates. To focus on ion outflows in the  
253 auroral zone and cusp, candidates in the subauroral zone or lower latitude, which were  
254 rare, were excluded. Details of this identification are described in Appendix A5.

255 Because the dataset (7 January 1998–5 February 1999) is very large, there are some  
256 candidates of outflow regions that is not appropriate to use. Data from the inbound or  
257 outbound part were not used for the statistical analysis if any of outflow regions met at  
258 least one of the following criteria:

- 259 1. The total time length of the outflow region was  $< 20$  s (4 data points).
- 260 2. Edges of the outflow region were located  $\leq 1^\circ$  in ILAT from the low and high  
261 latitude limit of the data.
- 262 3. A total of data gap periods of IESA or EESA around ( $\leq 1^\circ$  in ILAT from the edge)  
263 the outflow region exceeded 25% of the total time length of the data obtained in the  
264 outflow region.
- 265 4. Errors of the magnetic field data occurred (Appendix A2-1).

266 5. Any of the data points of the selected outflow region were obtained at <3000 km  
267 altitude.

268 This last criterion is set to limit the sampled range of altitude for the selected events  
269 and to avoid negative charging and high spacecraft velocity. Because the plasma density  
270 increases exponentially with decreasing altitude (Kitamura et al. 2009, 2011), the ion  
271 flux due to the ram effect increases drastically, and the ram effect creates an apparent  
272 flux increase at ~10 eV at low altitudes. This criterion also helps to reduce altitude  
273 dependence of the outflowing ion number fluxes above 10 eV. Although the field-  
274 aligned ion number fluxes are expected to be almost continuous in the direction of  
275 altitude on average at ~3000 km altitude where the local production is negligible, ions  
276 must have been energized to >10 eV at somewhere below the altitude of the satellite to  
277 exceed the lower energy limit (10 eV) of the present analysis. At low altitudes,  
278 outflowing ions below 10 eV may be dominant, and the outflowing ion number fluxes  
279 may be significantly underestimated due to the lower energy limit, if similar data  
280 obtained at very low altitudes. The limitation due to the lower energy limit of 10 eV is  
281 also discussed in Section 5.

282 We averaged ion number fluxes from IESA, electron densities in the loss cone, and  
283 Poynting fluxes of DC fields and Alfvénic waves during all candidates of the outflow  
284 region together in each inbound or outbound pass using the latitudinal width in ILAT in  
285 each 5 s data as the weight. By using this weight for the averaging, we can treat the data  
286 as if the satellite had crossed the auroral zone in the latitudinal direction with a constant  
287 velocity, regardless of its orbit, which usually crosses the auroral zone obliquely. The  
288 averaged data is counted as 1 event. The averaged SZA in each of these outflow events  
289 is calculated using the product of the latitudinal width in ILAT and the mapped ion  
290 number flux as the weight. The total number of these events was 1569. Poynting fluxes  
291 were available in 1448 events out of the total 1569 events (Appendix A2-2).

292

### 293 **3. SZA Dependence of Ion Number Fluxes**

294 Figure 2a indicates the outflowing ion number flux (mapped to 1000 km altitude) for  
295 various SZA values. Outflow events with large averaged fluxes ( $>10^8 \text{ cm}^{-2} \text{ s}^{-1}$ ) occurred  
296 mostly under sunlit ionospheric conditions ( $\text{SZA} < 90^\circ$ ), although events during high  
297 geomagnetic activity (large  $Kp$  index) occurred also under dark conditions. This result

298 indicates that the effect of the solar illumination (likely high ionospheric density and/or  
299 large scale height owing to high plasma temperature (Kitamura et al. 2011)) is important  
300 for the occurrence of ion outflows with large number fluxes. This result is consistent  
301 with the seasonal dependence of ion outflow discussed by Yau et al. (1985), which  
302 indicates that more  $O^+$  outflow occurs in summer than winter. Note that the outflowing  
303 ion flux in Figure 2a cannot simply be considered as averaged fluxes for specific  $Kp$   
304 levels, since events of small ( $<10^7 \text{ cm}^{-2} \text{ s}^{-1}$ ) ion number fluxes could not be included in  
305 the statistics.

306 Only the events near noon (0800–1600 magnetic local time (MLT)) are plotted in  
307 Figure 2b. The events that include any data point (before averaging) outside of the  
308 0800–1600 MLT range are not plotted. The figure shows that most of the events with  
309 large ion number fluxes occurred near noon. In contrast, the lack of ion outflow events  
310 with large number fluxes near midnight (2000–2400 or 0000–0400 MLT) (Figure 2c) is  
311 consistent with the importance of solar illumination for the occurrence of ion outflows  
312 with large number fluxes. Because the auroral zone around midnight is rarely  
313 illuminated by the sun, presumably it is difficult to drive ion outflow with large number

314 fluxes around midnight. As described in section 2, the orbital plane of the FAST satellite  
315 tended to be aligned to the noon-midnight meridian when the apogee stayed near the  
316 pole. Thus, auroral oval crossings are concentrated around noon and midnight. Because  
317 the overlap (around SZA of  $100^\circ$ ) of events around noon and midnight is limited, it is  
318 difficult to investigate the difference in the empirical relation around noon and that  
319 around midnight at the same SZA. Detailed analysis of the MLT effect is beyond the  
320 scope of the present study.

321 Shillings et al. (2017, 2018) investigated  $O^+$  ion outflows during large geomagnetic  
322 storms using data obtained by the Cluster spacecraft as extreme cases, and reported  
323 large magnitudes of  $O^+$  number flux (event mean) of  $3.5 \times 10^7 - 2 \times 10^9 \text{ cm}^{-2} \text{ s}^{-1}$   
324 (mapped to an ionospheric reference altitude with a magnetic field intensity of 50,000  
325 nT). The largest value of  $2 \times 10^9 \text{ cm}^{-2} \text{ s}^{-1}$  corresponds to  $\sim 1.5 \times 10^9 \text{ cm}^{-2} \text{ s}^{-1}$  at 1000 km  
326 altitude (a magnetic field intensity of  $\sim 37,000$  nT (Engwall et al. 2009)). Even this flux  
327 in an extreme case is within the range covered by the dataset used in the present study.

328

329 **4. SZA Dependence of the Empirical Relation between Energy Inputs and the Ion**

## 330 **Number Flux**

### 331 **4.1. Empirical Formula**

332 Energy inputs (electron density in the loss cone, precipitating electron density  
333 proposed by Strangeway et al. (2005), DC and Alfvén Poynting fluxes) were  
334 logarithmically averaged using bins of the ion number flux (one order of magnitude was  
335 divided by 10 bins). The total latitudinal widths in ILAT of the outflow events were  
336 used as the weight for this averaging. The logarithmically averaged values were fitted  
337 with a weighted least squares method using the following formula:

$$338 \quad F_i = 10^a x^b, \quad (1)$$

339 where  $F_i$  is the ion number flux (mapped to 1000 km altitude) in  $\text{cm}^{-2} \text{s}^{-1}$ ,  $x$  is the  
340 energy input, and  $a$  and  $b$  are free parameters determined by the fitting. This fitting  
341 formula is the same as that used by Strangeway et al. (2005) and Brambles et al. (2011).  
342 In this fitting, the sum of the total latitudinal widths in ILAT of the outflow events was  
343 used as the weight. The parameters selected as the energy input are those studied by  
344 Strangeway et al. (2005) and Brambles et al. (2011) and found that there are good  
345 correlations with outflowing ion fluxes. The use of other energy input parameters, to

346 find which input parameter is good, and to investigate the functional shape are beyond  
347 scope of the present study.

348 As described above, we used logarithmically averaged energy inputs, not the outflow  
349 events themselves, for this fitting for the following reason, because the ion number  
350 fluxes used here are biased by the lower flux limit ( $10^7 \text{ cm}^{-2} \text{ s}^{-1}$ ), which was used for  
351 event identification. Thus, in cases of small energy inputs, only cases in which the ion  
352 flux exceeded  $10^7 \text{ cm}^{-2} \text{ s}^{-1}$  were included for evaluation of the average energy input,  
353 despite that there must be cases where such a small energy input can cause ion outflows  
354 with the ion flux  $<10^7 \text{ cm}^{-2}$  in reality. This limitation would uplift the small energy  
355 input part of the regression line, and makes the gradient of the line unrealistically  
356 gradual, if each of the outflow events were used for the fitting. Instead, the use of the  
357 averaged energy inputs for each level of the ion number flux helps us avoid such a bias,  
358 particularly for small energy input cases.

#### 359 **4.2. Empirical Relations between the Electron Density in the Loss Cone and the** 360 **Ion Number Flux**

361 The electron density in the loss cone is defined as the partial electron density at the

362 location of the satellite using 4 pitch angle bins around the precipitating direction (the  
363 center of pitch angle bins ranges from  $-22.5^\circ$  to  $22.5^\circ$  (Northern hemisphere) or from  
364  $157.5^\circ$  to  $202.5^\circ$  (Southern hemisphere).

365 Figure 3 shows the relations between the electron density in the loss cone ( $n_{e\_lc}$ ) in  
366  $\text{cm}^{-3}$  ( $>50$  eV) and the mapped ion number flux. The width of the SZA bins is  $40^\circ$ , and  
367 neighboring bins overlap in half ( $20^\circ$ ) to include a larger number of events in each SZA  
368 bin. The empirical formulas were derived as follows.

369 SZA  $45^\circ$ – $85^\circ$ :  $F_i = 10^{9.162} n_{e\_lc}^{3.185}$  (2)

370 SZA  $65^\circ$ – $105^\circ$ :  $F_i = 10^{9.014} n_{e\_lc}^{2.686}$  (3)

371 SZA  $85^\circ$ – $125^\circ$ :  $F_i = 10^{8.643} n_{e\_lc}^{1.693}$  (4)

372 SZA  $105^\circ$ – $145^\circ$ :  $F_i = 10^{8.419} n_{e\_lc}^{1.100}$  (5)

373 The fitted line tends to become less steep with increasing SZA. The ion outflow  
374 events with small averaged number fluxes ( $\sim 10^7 \text{ cm}^{-2} \text{ s}^{-1}$ ) occur with smaller electron  
375 densities ( $\sim 5 \times 10^{-2} \text{ cm}^{-3}$ ) at large SZA, while ion outflow events with large number  
376 fluxes ( $> 10^8 \text{ cm}^{-2} \text{ s}^{-1}$ ) occur infrequently even in cases of high electron densities ( $> 5 \times$   
377  $10^{-1} \text{ cm}^{-3}$ ). Above the electron density of  $\sim 4 \times 10^{-1} \text{ cm}^{-3}$  (the ion number flux of  $\sim 1 \times$

378  $10^8 \text{ cm}^{-2} \text{ s}^{-1}$ ), the ion outflow flux given by the empirical formulas (Equations 2–5)  
379 decreases with increasing SZA at a certain magnitude of the electron density (Figure  
380 3e). The exponents ( $b$ ) of Equations 2 and 3 under sunlit conditions are slightly larger  
381 than those derived by Strangeway et al. (2005) (their Equation 4,  $b = 2.240$ ).

### 382 **4.3. Empirical Relations between the Precipitating Electron Density and the Ion** 383 **Number Flux**

384 Strangeway et al. (2005) suggested the precipitating electron density ( $n_{\text{ep}}$ ), which has  
385 the dimensions of the number density in  $\text{cm}^{-3}$  defined as

$$386 \quad n_{\text{ep}} = 2.134 \times 10^{-14} f_{\text{en}}^{3/2} / f_{\text{ee}}^{1/2}, \quad (6)$$

387 where  $f_{\text{en}}$  is the averaged field-aligned (downward positive) electron number flux ( $>50$   
388 eV) in  $\text{cm}^{-2} \text{ s}^{-1}$ , and  $f_{\text{ee}}$  is the averaged field-aligned electron energy flux ( $>50$  eV) in  
389  $\text{mW m}^{-2}$ . Note that these fluxes are mapped to 1000 km altitude in the present study,  
390 while Strangeway et al. (2005) used local ones ( $\sim 4000$  km altitude). Thus, the  
391 precipitating electron density is  $\sim 2.9$  times larger than that used by Strangeway et al.  
392 (2005) under the same condition. Positive values indicate downward fluxes. This  
393 precipitating electron density is presumably more useful for modeling studies than the

394 electron density in the loss cone, since the precipitating electron density can be  
395 calculated using electron fluxes mapped along field lines.

396 If the averaged energy flux and/or the averaged number flux were negative (upward),  
397 the precipitating electron density became negative (11 events) or imaginary numbers  
398 (40 events). Even after excluding such invalid cases, 1453 out of 1504 events (97.6%)  
399 remained available for this statistical analysis. All excluded events except one have  
400 negative averaged number fluxes, which were significantly affected by upgoing low-  
401 energy electron beams (Ergun et al. 1998; Elphic et al. 2000; Andersson and Ergun  
402 2006) in the region of ion outflow events. Most of these events occurred at large SZA  
403 ( $>100^\circ$ ), which is consistent with the seasonal dependence of upward electron beams  
404 (Elphic et al. 2000).

405 The SZA dependence of the relations between the precipitating electron density and  
406 the ion number flux are shown in Figure 4. The result is quite similar to that between  
407 the electron density in the loss cone and the ion number flux (Figure 3), although the  
408 scatter of data points tends to be larger. The empirical formulas between the  
409 precipitating electron density ( $>50$  eV) and the mapped ion number flux are derived as

410 listed below.

411 SZA 45°–85°:  $F_i = 10^{8.069} n_{\text{ep}}^{2.984}$  (7)

412 SZA 65°–105°:  $F_i = 10^{8.259} n_{\text{ep}}^{2.208}$  (8)

413 SZA 85°–125°:  $F_i = 10^{8.391} n_{\text{ep}}^{1.578}$  (9)

414 SZA 105°–145°:  $F_i = 10^{8.484} n_{\text{ep}}^{1.185}$  (10)

415 Below the precipitating electron density of  $\sim 1.5 \text{ cm}^{-3}$  (the ion number flux of  $\sim 6 \times$   
416  $10^8 \text{ cm}^{-2} \text{ s}^{-1}$ ), the ion outflow flux given by the empirical formulas (Equations 7–10)  
417 increases with increasing SZA at a certain magnitude of the precipitating electron  
418 density (Figure 4e). The ion number flux given by these formulas tends to be slightly  
419 smaller than that derived by Strangeway et al. (2005) (their Equation 3 after the  
420 altitudinal correction) under sunlit conditions.

#### 421 **4.4. Empirical Relations between the DC Poynting Flux and the Ion Number**

#### 422 **Flux**

423 We excluded cases in which the averaged DC Poynting flux was negative (upward),  
424 and 1389 out of 1448 events (95.9%) remained available for this statistical analysis.  
425 Most of the excluded events (46 out of 59) occurred at large SZA ( $>95^\circ$ ).

426 The relation between the DC Poynting flux and the ion number flux does not show  
427 clear SZA dependence, as seen from Figure 5. The fitted functions are similar, but the  
428 large Poynting flux events tend to occur more under sunlit conditions than under dark  
429 conditions. Most of the averaged values of the DC Poynting flux in each flux bin at  
430 various SZA ranges are within the error bars (standard deviations) in the flux range  
431 where a significant number of events are present even at large SZAs. The empirical  
432 formulas between  $S_{DC}$  (mapped DC Poynting flux in  $\text{mW m}^{-2}$ ) and the mapped ion  
433 number flux are derived as listed below.

$$434 \quad \text{SZA } 45^\circ\text{--}85^\circ: F_i = 10^{6.792} S_{DC}^{1.757} \quad (11)$$

$$435 \quad \text{SZA } 65^\circ\text{--}105^\circ: F_i = 10^{7.162} S_{DC}^{1.423} \quad (12)$$

$$436 \quad \text{SZA } 85^\circ\text{--}125^\circ: F_i = 10^{7.398} S_{DC}^{1.323} \quad (13)$$

$$437 \quad \text{SZA } 105^\circ\text{--}145^\circ: F_i = 10^{7.298} S_{DC}^{1.822} \quad (14)$$

438 Since the exponents did not show any systematic SZA dependence, we also  
439 calculated a regression line using all the events without classification of SZA.

$$440 \quad \text{SZA } 45^\circ\text{--}145^\circ: F_i = 10^{7.218} S_{DC}^{1.499} \quad (15)$$

441 The ion number fluxes from these formulas are roughly comparable to that from the

442 empirical formula derived by Strangeway et al. (2005) (their Equation 5 after the  
443 altitudinal correction) (Figure 5f).

#### 444 **4.5. Empirical Relations between the Alfvén Poynting Flux and the Ion Number** 445 **Flux**

446 After the exclusion of cases in which the averaged Alfvén Poynting flux was negative  
447 (upward), 1267 out of 1448 events (87.5%) remained available for this statistical  
448 analysis. Excluded events were not strongly concentrated to large SZAs (104 out of 181  
449 at large SZAs ( $>95^\circ$ )) as compared with that in the cases of the DC Poynting flux.

450 Similar to the relations between the DC Poynting flux and the ion number flux  
451 (Figure 5 and Equations 11–14), the relation between the Alfvén Poynting flux and the  
452 ion number flux does not show clear SZA dependence in the flux range where a large  
453 number of events are present, as seen from Figure 6. The empirical formulas between  
454  $S_A$  (mapped Alfvén Poynting flux in  $\text{mW m}^{-2}$ ) and the mapped ion number flux are  
455 derived as listed below.

$$456 \text{ SZA } 45^\circ\text{--}85^\circ: F_i = 10^{10.780} S_A^{1.432} \quad (16)$$

$$457 \text{ SZA } 65^\circ\text{--}105^\circ: F_i = 10^{10.749} S_A^{1.493} \quad (17)$$

458 SZA 85°–125°:  $F_i = 10^{10.418} S_A^{1.360}$  (18)

459 SZA 105°–145°:  $F_i = 10^{10.026} S_A^{1.178}$  (19)

460 We also calculated a regression line using all the events without classification of SZA.

461 SZA 45°–145°:  $F_i = 10^{11.062} S_A^{1.656}$  (20)

462 The ion number fluxes from these formulas are roughly comparable to that from the  
463 empirical formula derived by Brambles et al. (2011) (after the altitudinal correction)  
464 (Figure 6f).

465

## 466 5. Discussion

467 The new empirical formulas derived in the present study include information about  
468 the SZA effect. This new information is valuable for investigating day-night and/or  
469 interhemispheric asymmetries (around solstice) of ion outflows in global  
470 magnetospheric models. Since the solar activity level (monthly mean  $F_{10.7}$  index) from  
471 January 1998 to February 1999 was almost the same as the latest solar maximum (Solar  
472 cycle 24), the empirical formulas obtained in the present study should be applicable to  
473 comparisons of the ion composition in the magnetosphere between the global models

474 and measurements by the Van Allen Probes and the Magnetospheric Multiscale

475 missions. Effects of solar activity will be studied in the future.

476 It is still impossible to determine the dominant energy input for the outflowing ion  
477 flux among the four on the basis of empirical formulas. One may think that the Poynting  
478 fluxes have a strong contribution, because the empirical formulas between the Poynting  
479 fluxes and ion number fluxes do not strongly depend on SZA. The error bars, which  
480 often spreads about an order of magnitude of the Poynting fluxes at a certain ion  
481 number flux (Figures 3 and 4), however, tend to be larger than those of electron  
482 precipitation, which is usually within a factor of  $\sim 3$ – $5$  (Figures 5 and 6).

483 Since the low-energy ions have limited upward velocities (order of  $10 \text{ km s}^{-1}$ ), it  
484 takes at least several minutes for them to reach the altitude of 4000 km from the  
485 ionosphere. Thus, the energy inputs to the ionosphere at least several minutes before the  
486 satellite observations may be most relevant to the observed ion number fluxes at  $\sim 4000$   
487 km altitude. Observations by the Cluster spacecraft indicate that the  $\text{O}^+$  ion number flux  
488 fluctuates on the timescale of several minutes (Bouhram et al. 2004; Nilsson et al.  
489 2008). This would imply that energy inputs that drive outflows also have fluctuations

490 with similar timescales. Such fluctuations may explain the large error bars in Figures 3–  
491 6. Nevertheless, the present results are based on a substantial number of events and we  
492 believe that the empirical relations can provide the average profile of ion outflow for  
493 varying energy inputs, which is readily usable for global magnetospheric simulations.

494 Even if the energy input is constant after a certain onset time, the outflowing O<sup>+</sup> ion  
495 number flux increases dramatically in the initial ~10 min after the driving forces turned  
496 on in the models (Su et al. 1999; Horwitz and Zeng 2009). Whereas this time scale  
497 would change if different settings of the driving force are used, the duration of energy  
498 inputs would also contribute to the large deviation. If the intensity and duration of  
499 energy inputs are enough to modify and control the conditions of background plasma,  
500 SZA dependence would almost disappear (Horwitz and Zeng, 2009). That is, however,  
501 not the case for at least some events, because the empirical relation of the electron  
502 density in the loss cone or precipitating electron density and the outflowing ion number  
503 flux shows SZA dependence.

504 A combination of a latitudinally narrow cusp (Meng 1982, 1983; Kitamura et al.  
505 2010a) and fast ionospheric convection during the main phase of geomagnetic storms

506 causes ion energization with a short duration in a certain flux tube. In such cases, the  
507 duration of energization and the time-lag discussed above would be especially important  
508 (Varney et al. 2015) in addition to the energy input and SZA. The derived empirical  
509 relations would also be averaged characteristics from the perspective of a limited  
510 duration of ion energization.

511 Note that only ions above 10 eV are included in the present study. Since transverse  
512 energization of ions also occurs above ~4000 km altitude (Peterson et al. 1992; Miyake  
513 et al. 1993), the ion number flux above 10 eV for higher altitudes (for example, the  
514 inner boundary of magnetospheric simulations) is probably underestimated. During  
515 geomagnetic storms, O<sup>+</sup> ion outflows with energies below ~10 eV with very large fluxes  
516 ( $>10^9 \text{ cm}^{-2} \text{ s}^{-1}$  mapped to 1000 km altitude) are present poleward of the cusp (observed  
517 at ~9000 km altitude) (Kitamura et al. 2010b). Such a population was not included in  
518 the present analysis owing to the difficulty in use of ion data below 10 eV, although how  
519 often such component becomes significant still remains as an open question, due to the  
520 lack of detailed ion observations below ~10 eV. This will become an important subject  
521 of observations in future missions.

522 As discussed in the introduction, empirical relations between energy inputs and ion  
523 outflow fluxes have been used as the boundary conditions of O<sup>+</sup> ions at the inner  
524 boundary in global magnetospheric simulations (Fok et al. 2006, 2011; Moore et al.  
525 2007, 2010; Brambles et al. 2010, 2011, 2013; Damiano et al. 2010; Perroomian et al.  
526 2011; Ouellette et al. 2013). However, it is not clear whether O<sup>+</sup> ions are dominant in  
527 many cases, because there are many observations of ion outflows with H<sup>+</sup> ion fluxes  
528 larger than O<sup>+</sup> ion fluxes (Tung et al. 2001; Peterson et al. 2001, 2006; Andersson et al.  
529 2004; Wilson et al. 2004; Maes et al. 2015). The polar wind is present as thermal energy  
530 ion outflows (e.g., Yau et al. 2007 and references therein). Observational studies by  
531 Kitamura et al. (2016) showed that upward velocity of O<sup>+</sup> ions are almost zero at least  
532 up to ~7000 km altitude in the sunlit polar cap region under geomagnetically quiet  
533 condition (the region and condition where very small auroral energy input are  
534 expected), while H<sup>+</sup> ions have upward velocity at least above ~3000 km altitude. This  
535 fact clearly indicates that H<sup>+</sup> ion outflows (polar wind type) do not need strong energy  
536 input, in contrast to O<sup>+</sup> ion outflows. As for such H<sup>+</sup> ions, different types of recent  
537 satellite observations (direct thermal energy ion measurements and estimations of

538 components masked by spacecraft potential (Huddleston et al. 2005), measurements of  
539 spacecraft potential and wake (Engwall et al. 2009; André et al. 2015), and estimations  
540 using photoelectron outflows (Kitamura et al. 2012, 2015)) indicate that the number  
541 flux of the polar wind is  $\sim 2 \times 10^8 \text{ cm}^{-2} \text{ s}^{-1}$  (mapped to 1000 km altitude). This flux is  
542 larger than that for most of the events (especially for geomagnetically quiet periods)  
543 shown in Figure 2. This polar wind type outflow is expected to exist also at the auroral  
544 zone. Thus, if background (polar wind)  $\text{H}^+$  ions can be accelerated up to 10 eV,  
545 additional  $\text{O}^+$  ions may not be necessary for driving ion outflows with small fluxes  
546 ( $< 10^8 \text{ cm}^{-2} \text{ s}^{-1}$ ). Analyses that use mass resolved data (for example, the data from the  
547 Time-of-flight Energy, Angle, Mass Spectrograph (TEAMS) instrument on the FAST  
548 satellite (Klumpar et al. 2001), which are under re-calibration (Zhao et al. 2020)) will be  
549 important in the future, probably especially for ion outflow events with small fluxes.

550

## 551 **6. Summary and Conclusions**

552 To understand how strongly ionospheric conditions (sunlit or dark) affect ion  
553 outflows, we derived empirical formulas between energy inputs (electron density in the

554 loss cone ( $>50$  eV), precipitating electron density ( $>50$  eV), mapped DC and Alfvén  
555 Poynting fluxes) and outflowing ion number fluxes (mapped to 1000 km altitude) for a  
556 wide range of SZA ( $45^\circ$ – $145^\circ$ ), using data obtained by the FAST satellite (3000–4150  
557 km altitude) from 7 January 1998 to 5 February 1999 (monthly mean  $F_{10.7}$  index of  
558 93.4–150.1).

559 Ion outflow events with large averaged fluxes ( $>10^8$  cm<sup>-2</sup> s<sup>-1</sup>) occur mostly under  
560 sunlit ionospheric conditions (SZA  $< 90^\circ$ ). Thus, the effect of the solar illumination  
561 (presumably high ionospheric density and/or large scale height owing to high plasma  
562 temperature) probably plays an important role in the occurrence of ion outflows with  
563 large averaged fluxes.

564 Empirical relations between the electron density in the loss cone ( $>50$  eV) or  
565 precipitating electron density ( $>50$  eV) and the outflowing ion number fluxes show  
566 clear dependence on SZA at the ionospheric footprint. The outflowing ion number flux  
567 increases with increasing electron density in the loss cone and precipitating electron  
568 density, and the gradient of empirical formulas becomes less steep with increasing SZA.  
569 SZA dependence was not seen in the empirical relations between the Poynting fluxes

570 (DC and Alfvén) and the outflowing ion number flux. Note that the electric fields  
571 perpendicular to the velocity vector of the satellite are not derived owing to the lack of  
572 reliable measurements of the electric fields along the spin axis. Thus, the magnitude of  
573 the Poynting fluxes is probably underestimated, and this incomplete Poynting flux  
574 measurement probably contributes to somewhat large scatter of the data points in the  
575 present analyses on the relationship between the Poynting fluxes and the ion flux.

576 Ionospheric conditions (sunlit or dark) affect ion outflows. Under dark ionospheric  
577 conditions, although weak electron precipitation can drive ion outflows with small  
578 averaged fluxes ( $\sim 10^7 \text{ cm}^{-2} \text{ s}^{-1}$ ), it is hard to drive intense ion outflows ( $> 10^8 \text{ cm}^{-2} \text{ s}^{-1}$ )  
579 presumably owing to low ionospheric  $\text{O}^+$  ion densities and/or a small scale height of  $\text{O}^+$   
580 ions.

581

## 582 **Appendix**

### 583 **A1. Calculation and Subtraction of Background of IESA**

584 Background counts of IESA were subtracted from IESA data using count rates in the  
585 source cone. Although the method of background subtraction was basically similar to

586 that of Yao et al. (2008a, 2008b), we only used IESA data to derive the background  
587 count rate, since the background count rates of IESA were slightly different from that of  
588 EESA. Another difference from the method of background subtraction by Yao et al.  
589 (2008a, 2008b) is that the background count rate was calculated by a linear least-  
590 squares fitting using a moving window (25 s) for better handling of the data with  
591 various time resolutions, while they used boxcar averaged ones. This calculation was  
592 performed after the removals of spikes, which were presumably caused by erroneous  
593 data.

594

## 595 **A2. Rejection of Erroneous Data**

### 596 **A2.1. Magnetic Field Data**

597 In some cases, processed magnetic field data are apparently incorrect. To remove  
598 such incorrect data quantitatively as much as possible, the outflow events that satisfied  
599 the following two criteria at any of the 5 s averaged data points in the outflow regions  
600 were excluded from the present statistical analyses.

601 1. The magnetic field intensity that was calculated from observed data differs from

602 that from the IGRF model by  $>10\%$ .

603 2. The direction of the magnetic field differs from that calculated using the IGRF  
604 model by  $>5^\circ$ .

605 Additionally, two events were excluded by visual inspection of the magnetic field  
606 data.

### 607 **A2.2. Electric Field Data**

608 Sometimes an unusually large electric field was recorded just after a data gap. Thus,  
609 if there was any gap in the electric field data, the 5 s averaged Poynting flux at the  
610 period was not used. If Poynting fluxes were not available at any of data points in the  
611 outflow regions, the event was excluded from the statistical analyses in Sections 4.4 and  
612 4.5.

### 613 **A2.3. Ion and Electron Data**

614 Sometimes ion or electron data are apparently incorrect. The ion data were excluded  
615 if counts at all pitch angle bins of IESA in one third (top, middle, or bottom) of the  
616 energy bins were zero. This is the most typical type of the error. The counts do not  
617 become zero at such a large number of bins in the correct data (Figures 1a and 1b).

618 Frequently, another type of error occurs just after the change of the observational  
619 modes: Slow survey ( $\sim 2.5$  s resolution) and Fast survey ( $\sim 0.625$  or  $\sim 0.3125$  s  
620 resolution). Seven (two) data points were excluded after the change to Fast (Slow)  
621 survey mode. This number was determined by visual inspection. The same rejection  
622 processes were also applied to electron data.

623

### 624 **A3. Periods of Significant Negative Spacecraft Charging**

625 If the spacecraft is charged negatively, thermal energy ions are attracted from all  
626 directions. A 5 s period (one averaged data point) was regarded as a period of significant  
627 spacecraft charging, if there was at least one energy bin (4–70 eV) that the differential  
628 energy fluxes exceeded  $5 \times 10^6 \text{ eV}^{-1} \text{ cm}^{-2} \text{ s}^{-1} \text{ sr}^{-1} \text{ eV}^{-1}$  in all of the four pitch angle  
629 ranges:  $-16.875^\circ$ – $16.875^\circ$ ,  $40^\circ$ – $140^\circ$ ,  $163.125^\circ$ – $196.875^\circ$ , and  $220^\circ$ – $320^\circ$ . The adjacent  
630 5 s periods are also excluded for safety: some of data before averaging may be affected  
631 by the charging. By visual inspections of all outflow events, this definition is enough to  
632 exclude intervals of significant spacecraft charging with large ion number fluxes that  
633 can strongly affect the identification of outflow events. The upper energy limit of 70 eV

634 is to avoid misidentification in the cusp in cases where ion precipitation was so intense  
635 that the differential energy flux exceeded  $5 \times 10^6 \text{ eV}^{-1} \text{ cm}^{-2} \text{ s}^{-1} \text{ sr}^{-1} \text{ eV}^{-1}$  even in the  
636 source cone owing to pitch angle scattering.

637

#### 638 **A4. Identification of the Polar Cap**

639 The polar cap was defined with the use of 5 s averaged low-energy ion data (110 eV–  
640 24 keV), according to the threshold of a mean differential energy flux ( $<10^{4.6} \text{ eV}^{-1} \text{ cm}^{-2}$   
641  $\text{ s}^{-1} \text{ sr}^{-1} \text{ eV}^{-1}$ ) described by Andersson et al. (2004). The mean differential energy flux  
642 was calculated by using pitch angle ranges of  $-30^\circ$ – $30^\circ$ ,  $150^\circ$ – $210^\circ$ , and  $40^\circ$ – $140^\circ$  or  
643  $220^\circ$ – $320^\circ$ . In some orbits, contamination caused by solar radiation increases count  
644 rates around  $90^\circ$  or  $270^\circ$  at high latitudes. Because this increase affects the  
645 identification of the polar cap, the mean differential energy flux in the pitch angle range  
646 of  $40^\circ$ – $140^\circ$  or  $220^\circ$ – $320^\circ$ , whichever smaller, is selected to avoid this contamination  
647 (Kitamura et al. 2015). Continuous ( $\geq 10$  s,  $\geq 2$  data points) periods in which the mean  
648 differential energy flux met the criterion were selected as candidates of the polar cap.  
649 Sometimes this criterion was satisfied for data obtained in the subauroral zone. To

650 exclude such cases, the candidates that are connected to the region where energetic ions  
651 ( $>4$  keV) show double loss cones (Appendix A5) without a data gap of  $\geq 60$  s or  
652 equatorward of such regions were excluded. In some cases, short candidates that were  
653 appeared between the auroral zone and the region of the double loss cone could not be  
654 excluded. There were some cases in which the region of double loss cone was not  
655 identified and candidates in the subauroral zone could not be excluded. All these two  
656 types of cases, however, had polar cap periods much longer than 200 s, and thus the  
657 overlooking did not affect the exclusion of the outflow events.

658 Although contamination owing to solar radiation causes increase in count rates, the  
659 increase occurs around the pitch angle of  $90^\circ$  at high latitudes. Thus, this does not  
660 strongly affect the calculations of field-aligned ion fluxes in the outflow regions ( $>10^7$   
661  $\text{cm}^{-2} \text{s}^{-1}$ ). This is one of the reasons why we set the lower flux limit to identify the  
662 outflow regions. In some cases, the contamination causes the apparent field-aligned ion  
663 fluxes of the order of  $10^6 \text{ cm}^{-2} \text{ s}^{-1}$  (mapped to 1000 km altitude). To treat ion outflows  
664 with fluxes smaller than  $\sim 10^7 \text{ cm}^{-2} \text{ s}^{-1}$  in the future, this apparent flux must be  
665 corrected.

666

667 **A5. Identification of Double Loss Cones and the Subauroral Zone**

668 Identification of regions of double loss cones was performed if the mean differential  
669 energy flux of ions above 4 keV in the pitch angle ranges of  $40^\circ$ – $140^\circ$  and  $220^\circ$ – $320^\circ$   
670 (trapped population) were larger than  $10^{4.6} \text{ eV}^{-1} \text{ cm}^{-2} \text{ s}^{-1} \text{ sr}^{-1} \text{ eV}^{-1}$ . The periods of  
671 double loss cones were defined as cases where the mean differential energy flux above 4  
672 keV near the center of the loss cone (in the pitch angle range from  $163.125^\circ$  to  $196.875^\circ$   
673 (Northern Hemisphere) or from  $-16.875^\circ$  to  $16.875^\circ$  (Southern Hemisphere)) was lower  
674 than 50% of those in the pitch angle ranges of  $40^\circ$ – $140^\circ$  and  $220^\circ$ – $320^\circ$ . Examples are  
675 shown above Figure 1 with red bars. Even if there were data gaps in the interval of  
676 double loss cones, the interval was treated as one continuous interval ( $\sim 1940$  UT). To  
677 avoid misidentifications, short intervals (1 or 2 data points with double loss cones) were  
678 excluded.

679 Very energetic ion conics that extended above 4 keV could be misidentified as a  
680 region of double loss cones, although such cases were very rare at this altitude. Thus, in  
681 the case in which the ion number flux above 4 keV exceeded  $10^6 \text{ cm}^{-2} \text{ s}^{-1}$  (mapped to

682 1000 km altitude), the region was treated as the region of double loss cones only if both  
683 sides of the case satisfied the criteria of double loss cones.

684 The region of  $ILAT < 45^\circ$  or high background count rates ( $>50$  counts/s) that were  
685 connected to  $ILAT < 65.9^\circ$  ( $L < 6$ ) were removed (marked as subauroral zone). In this  
686 removal, even if there were data gaps in the interval of high background count rates, the  
687 interval was regarded as connected. To focus on outflows in the auroral zone, the  
688 poleward boundary of the most equatorward region of double loss cones in the  
689 remaining part of the inbound or outbound pass was selected as the equatorward  
690 boundary of the region for the analyses (poleward of the subauroral zone). Examples of  
691 the identified subauroral zones are shown above Figure 1 with black bars.

692

## 693 **Declarations**

694 **Ethics approval and consent to participate**

695 Not applicable

696 **Consent for publication**

697 Not applicable

698

### **List of abbreviations**

699

EESA: Electron spectrometers; FAST: Fast Auroral Snap shot; IESA:

700

Ion spectrometers; IGRF: International Geomagnetic Reference Field;

701

ILAT: Invariant latitude; MLT: Magnetic local time; SZA: Solar zenith

702

angle.

703

### **Availability of data and materials**

704

The  $K_p$  index were provided by WDC for Geomagnetism, Kyoto. The

705

EESA and IESA data and software for reading the data are available at

706

<http://sprg.ssl.berkeley.edu/data/fast/software/>. The software for getting

707

and reading the MGF and orbit data are available at

708

<http://sprg.ssl.berkeley.edu/fast/scienceops/fastidl.html>. The monthly

709

mean  $F_{10.7}$  solar radio flux index was provided by NGDC

710

([http://www.ngdc.noaa.gov/stp/space-weather/solar-data/solar-](http://www.ngdc.noaa.gov/stp/space-weather/solar-data/solar-features/solar-radio/noontime-flux/penticton/penticton_observed/listings/listing_drao_noontime-flux-observed_monthly.txt)

711

[features/solar-radio/noontime-](http://www.ngdc.noaa.gov/stp/space-weather/solar-data/solar-features/solar-radio/noontime-flux/penticton/penticton_observed/listings/listing_drao_noontime-flux-observed_monthly.txt)

712

[flux/penticton/penticton\\_observed/listings/listing\\_drao\\_noontime-flux-](http://www.ngdc.noaa.gov/stp/space-weather/solar-data/solar-features/solar-radio/noontime-flux/penticton/penticton_observed/listings/listing_drao_noontime-flux-observed_monthly.txt)

713

[observed\\_monthly.txt](http://www.ngdc.noaa.gov/stp/space-weather/solar-data/solar-features/solar-radio/noontime-flux/penticton/penticton_observed/listings/listing_drao_noontime-flux-observed_monthly.txt)).

714 **Competing interests**

715 The authors declare that they have no competing interests.

716 **Funding**

717 NK was supported by a Research Fellowship of the Japan Society for the  
718 Promotion of Science (JSPS), JSPS KAKENHI Grant Number 24·5283.

719 NK was supported by Grant-In-Aid for Young Scientist 19K14781 from  
720 JSPS and MEXT of Japan. KS was supported by Grant-In-Aid for

721 Scientific Research (B) 24340118 from JSPS and MEXT of Japan. KK is  
722 supported by the GEMISIS project at STEL/Nagoya University. Part of

723 the work of KK and TH was done at the ERG-Science Center operated  
724 by ISAS/JAXA and ISEE/Nagoya University. The work of YN was

725 supported by NASA grant 80NSSC18K0657, 80NSSC20K0604 and  
726 80NSSC20K0725, NSF grant AGS-1907698, and AFOSR grant FA9559-

727 16-1-0364. EJL and LMK were supported by NASA grant  
728 80NSSC19K0073.

729 **Authors' contributions**

730 NK designed this study, performed the data analysis, and prepared the  
731 manuscript. RJS provided the magnetometer data of FAST. All authors  
732 attended scientific discussion and approved the final manuscript.

### 733 **Acknowledgements**

734 We acknowledge J. P. McFadden and C. W. Carlson for use of the EESA  
735 and IESA data of FAST (<http://sprg.ssl.berkeley.edu/data/fast/11/>).

736

737

### 738 **References**

739 Andersson L, Ergun RE (2006) Acceleration of antiearthward electron fluxes in the  
740 auroral region. *J Geophys Res* 111:A07203. <https://doi.org/10.1029/2005JA011261>

741 Andersson L, Peterson WK, McBryde KM (2004) Dynamic coordinates for auroral ion  
742 outflow. *J Geophys Res* 109:A08201. <https://doi.org/10.1029/2004JA010424>

743 André M., Li K, Eriksson AI (2015) Outflow of low-energy ions and the solar cycle. *J*  
744 *Geophys Res Space Phys* 120:1072–1085. <https://doi.org/10.1002/2014JA020714>

745 Barakat AR, Schunk RW (2006) A three-dimensional model of the generalized polar wind.

746 J Geophys Res 111:A12314. <https://doi.org/10.1029/2006JA011662>

747 Barakat AR, Eccles JV, Schunk RW (2015) Effects of geographic-geomagnetic pole offset  
748 on ionospheric outflow: Can the ionosphere wag the magnetospheric tail? Geophys  
749 Res Lett 42:8288–8293. <https://doi.org/10.1002/2015GL065736>

750 Bouhram M, Klecker B, Miyake W, Rème H, Sauvaud J-A, Malingre M, Kistler L, Blågău  
751 A (2004) On the altitude dependence of transversely heated O<sup>+</sup> distributions in the  
752 cusp/cleft. Ann Geophys 22(5):1787–1798. [https://doi.org/10.5194/angeo-22-1787-](https://doi.org/10.5194/angeo-22-1787-2004)  
753 2004

754 Bouhram M, Klecker B, Paschmann G, Haaland S, Hasegawa H, Blagau A, Rème H,  
755 Sauvaud JA, Kistler LM, Balogh A (2005) Survey of energetic O<sup>+</sup> ions near the  
756 dayside mid-latitude magnetopause with cluster. Ann Geophys 23(4):1281–1294.  
757 <https://doi.org/10.5194/angeo-23-1281-2005>

758 Brambles OJ, Lotko W, Daminao PA, Zhang B, Wiltberger M, Lyon J (2010) Effects of  
759 causally driven cusp O<sup>+</sup> outflow on the stormtime magnetosphere-ionosphere system  
760 using a multi-fluid global simulation. J Geophys Res 115:A00J04.  
761 <https://doi.org/10.1029/2010JA015469>

762 Brambles OJ, Lotko W, Zhang B, Wiltberger M, Lyon J, Strangeway RJ (2011)  
763 Magnetosphere sawtooth oscillations induced by ionospheric outflow. *Science*,  
764 332:1183–1186. <https://doi.org/10.1126/science.1202869>

765 Brambles OJ, Lotko W, Zhang B, Ouellette J, Lyon J, Wiltberger M (2013) The effects of  
766 ionospheric outflow on ICME and SIR driven sawtooth events. *J Geophys Res Space*  
767 *Phys* 118, 6026–6041. <https://doi.org/10.1002/jgra.50522>

768 Buchert SC, Ogawa Y, Fujii R, van Eyken AP (2004) Observations of diverging field-  
769 aligned ion flow with the ESR. *Ann Geophys* 22(3):889–899.  
770 <https://doi.org/10.5194/angeo-22-889-2004>

771 Cattell C, Dombeck J, Eskolin M, Hanson L, Lorshbough DE, Carlson CW, McFadden J,  
772 Temerin M (2013) FAST observations of solar illumination and solar cycle  
773 dependence of the acceleration of upflowing ion beams on auroral field lines. *J*  
774 *Geophys Res Space Phys*, 118:3203–3213. <https://doi.org/10.1002/jgra.50302>

775 Carlson CW, Pfaff RF, Watzin JG (1998) The Fast Auroral SnapshoT (FAST) Mission.  
776 *Geophys Res Lett* 25:2013–2016. <https://doi.org/10.1029/98GL01592>

777 Carlson, CW, McFadden JP, Turin P, Curtis DW, Magoncelli A (2001) The electron and

778 ion plasma experiment for FAST. *Space Sci Rev* 98:33–65.  
779 <https://doi.org/10.1023/A:1013139910140>

780 Cohen IJ, Mauk BH, Anderson BJ, Westlake JH, Sibeck DG, Giles BL, Pollock CJ,  
781 Turner DL, Fennell JF, Blake JB, Clemmons JH, Jaynes AN, Baker DN, Craft JV,  
782 Spence HE, Niehof JT, Reeves GD, Torbert RB, Russell CT, Strangeway RJ, Magnes  
783 W, Trattner KJ, Fuselier SA, Burch JL (2016) Observations of energetic particle  
784 escape at the magnetopause: Early results from the MMS Energetic Ion Spectrometer  
785 (EIS). *Geophys Res Lett* 43, 5960–5968. <https://doi.org/10.1002/2016GL068689>

786 Collin HL, Peterson WK, Lennartsson OW, Drake JF (1998) The seasonal variation of  
787 auroral ion beams. *Geophys Res Lett* 25:4071–4074.  
788 <https://doi.org/10.1029/1998GL900090>

789 Daglis IA (1997) The role of magnetosphere-ionosphere coupling in magnetic storm  
790 dynamics. In: Tsurutani BT, Gonzalez WD, Kamide Y, Arballo JK (ed) *Magnetic*  
791 *Storms*. Geophysical Monograph Series, vol 98, AGU, Washington, D. C., pp 107–  
792 115. <https://doi.org/10.1029/GM098p0107>

793 Damiano PA, Brambles OJ, Lotko W, Zhang B, Wiltberger M, Lyon J (2010) Effects of

794 solar wind dynamic pressure on the ionospheric O<sup>+</sup> fluence during the 31 August 2005  
795 storm. *J Geophys Res* 115:A00J07. <https://doi.org/10.1029/2010JA015583>

796 Demars HG, Schunk RW (2001) Seasonal and solar cycle variations of the polar wind. *J*  
797 *Geophys Res* 106:8157–8168. <https://doi.org/10.1029/2000JA000386>

798 Demars HG, Schunk RW (2002) Three-dimensional velocity structure of the polar wind.  
799 *J Geophys Res* 107(A9):1250. <https://doi.org/10.1029/2001JA000252>

800 Denton RE, Jordanova VK, Fraser BJ (2014) Effect of spatial density variation and O<sup>+</sup>  
801 concentration on the growth and evolution of electromagnetic ion cyclotron waves. *J*  
802 *Geophys Res Space Phys* 119:8372–8395. <https://doi.org/10.1002/2014JA020384>

803 Ebihara Y, Kasahara S, Seki K, Miyoshi Y, Fritz TA, Chen J, Grande M, Zurbuchen TH  
804 (2009) Simultaneous entry of oxygen ions originating from the Sun and Earth into the  
805 inner magnetosphere during magnetic storms. *J Geophys Res* 114:A05219.  
806 <https://doi.org/10.1029/2009JA014120>

807 Elphic RC, Bonnell J, Strangeway RJ, Carlson CW, Temerin M, McFadden JP, Ergun RE,  
808 Peria W (2000) FAST observations of upward accelerated electron beams and  
809 downward field-aligned current region. In Ohtani SI, Fujii R, Hesse M, Lysak RL (eds)

810 Magnetospheric Current Systems. Geophysical Monograph Series, vol. 118, AGU,  
811 Washington, D. C., pp 173–180.

812 Elphic RC, Means JD, Snare RC, Strangeway RJ, Kepko L, Ergun RE (2001) Magnetic  
813 field instruments for the Fast Auroral Snapshot Explorer. *Space Sci Rev* 98:151–168.  
814 [https://doi.org/10.1007/978-94-010-0332-2\\_6](https://doi.org/10.1007/978-94-010-0332-2_6)

815 Engwall E, Eriksson AI, Cully CM, André M, Puhl-Quinn PA, Vaith H, Torbert R (2009)  
816 Survey of cold ionospheric outflows in the magnetotail. *Ann Geophys* 27(8):3185–  
817 3201. <https://doi.org/10.5194/angeo-27-3185-2009>

818 Ergun RE, Carlson CW, McFadden JP, Mozer FS, Delory GT, Peria W, Chaston CC,  
819 Temerin M, Roth I, Muschietti L, Elphic R, Strangeway R, Pfaff R, Cattell CA,  
820 Klumpar D, Shelley E, Peterson W, Moebius E, Kistler L (1998) FAST satellite  
821 observations of large-amplitude solitary structures. *Geophys Res Lett* 25:2041–2044.  
822 <https://doi.org/10.1029/98GL00636>

823 Ergun RE, Carlson CW, Mozer FS, Delory GT, Temerin M, McFadden JP, Pankow D,  
824 Abiad R, Harvey P, Wilkes R, Primbsch H, Elphic R, Strangeway R, Phaff R, Cattell  
825 CA (2001) The FAST satellite fields instrument. *Space Sci Rev* 98:67–91.

826 [https://doi.org/10.1007/978-94-010-0332-2\\_3](https://doi.org/10.1007/978-94-010-0332-2_3)

827 Erlandson RE, Zanetti LJ (1998) A statistical study of auroral electromagnetic ion  
828 cyclotron waves. *J Geophys Res* 103:4627–4636. <https://doi.org/10.1029/97JA03169>

829 Finlay CC, Maus S, Beggan CD, Bondar TN, Chambodut A, Chernova TA, Chulliat A,  
830 Golovkov VP, Hamilton B, Hamoudi M, Holme R, Hulot G, Kuang W, Langlais B,  
831 Lesur V, Lowes FJ, Lühr H, Macmillan S, Manda M, McLean S, Manoj C, Menvielle  
832 M, Michaelis I, Olsen N, Rauberg J, Rother M, Sabaka TJ, Tangborn A, Tøffner-  
833 Clausen L, Thébault E, Thomson AWP, Wardinski I, Wei Z, Zvereva TI (2010)  
834 International Geomagnetic Reference Field: the eleventh generation. *Geophys J*  
835 *International*, 183:1216–1230. <https://doi.org/10.1111/j.1365-246X.2010.04804.x>

836 Fok MC, Moore TE, Brandt PC, Delcourt DC, Slinker SP, Fedder JA (2006) Impulsive  
837 enhancements of oxygen ions during substorms. *J Geophys Res* 111:A10222.  
838 <https://doi.org/10.1029/2006JA011839>

839 Fok MC, Moore TE, Slinker SP, Fedder JA, Delcourt DC, Nosé M, Chen SH (2011)  
840 Modeling the superstorm in November 2003. *J Geophys Res* 116:A00J17.  
841 <https://doi.org/10.1029/2010JA015720>

842 Foster C, Lester N, Davies JA (1998) A statistical study of diurnal, seasonal and solar  
843 cycle variations of F-region and topside auroral upflows observed by EISCAT  
844 between 1984 and 1996. *Ann Geophys* 16(10):1144–1158.  
845 <https://doi.org/10.1007/s00585-998-1144-0>

846 Fuselier SA, Mukherjee J, Denton MH, Petrinec SM, Trattner KJ, Toledo-Redondo S,  
847 André M, Aunai N, Chappell CR, Glocer A, Haaland S, Hesse M, Kistler LM,  
848 Lavraud B, Li WY, Moore TE, Graham D, Tenfjord P, Dargent J, Vines SK,  
849 Strangeway RJ, Burch JL (2019) High-density O<sup>+</sup> in Earth's outer magnetosphere and  
850 its effect on dayside magnetopause magnetic reconnection. *J Geophys Res Space Phys*  
851 124:10257–10269. <https://doi.org/10.1029/2019JA027396>

852 Garcia KS, Merkin VG, Hughes WJ (2010) Effects of nightside O<sup>+</sup> outflow on  
853 magnetospheric dynamics: results of multifluid MHD modeling. *J Geophys Res*  
854 115:A00J09. <https://doi.org/10.1029/2010JA015730>

855 Garner TW, Taylor BT, Gaussiran II TL, Coley WR, Hairston MR, Rich FJ (2010)  
856 Statistical behavior of the topside electron density as determined from DMSP  
857 observations: A probabilistic climatology. *J Geophys Res* 115:A07306.

858 <https://doi.org/10.1029/2009JA014695>

859 Glocer A, Tóth G, Gombosi T, Welling D. (2009a) Modeling ionospheric outflows and  
860 their impact on the magnetosphere, initial results. *J Geophys Res* 114:A05216.

861 <https://doi.org/10.1029/2009JA014053>

862 Glocer A, Tóth G, Ma Y, Gombosi T, Zhang JC, Kistler LM (2009b) Multifluid Block-  
863 Adaptive-Tree Solar wind Roe-type Upwind Scheme: Magnetospheric composition  
864 and dynamics during geomagnetic storms—Initial results. *J Geophys Res*  
865 114:A12203. <https://doi.org/10.1029/2009JA014418>

866 Glocer A, Kitamura N, Toth G, Gombosi T (2012) Modeling solar zenith angle effects on  
867 the polar wind. *J Geophys Res* 117:A04318. <https://doi.org/10.1029/2011JA017136>

868 Glocer A, Fok M, Meng X, Toth G, Buzulukova N, Chen S, Lin K (2013) CRCM +  
869 BATS-R-US two-way coupling. *J Geophys Res Space Phys* 118:1635–1650.  
870 <https://doi.org/10.1002/jgra.50221>

871 Glocer A, Toth G, Fok MC (2018) Including kinetic ion effects in the coupled global  
872 ionospheric outflow solution. *J Geophys Res Space Phys* 123:2851–2871.  
873 <https://doi.org/10.1002/2018JA025241>

874 Glocer A, Welling D, Chappell CR, Toth G, Fok MC, Komar C, Kang SB, Buzulukova  
875 N, Ferradas C, Bingham S, Mouikis C (2020) A case study on the origin of near-Earth  
876 plasma. *J Geophys Res Space Phys* 125:e2020JA028205.  
877 <https://doi.org/10.1029/2020JA028205>

878 Hamilton DC, Gloeckler G, Ipavich FM, Stüdemann W, Wilken B, Kremser G (1988)  
879 Ring current development during the great geomagnetic storm of February 1986. *J*  
880 *Geophys Res* 93:14343–14355. <https://doi.org/10.1029/JA093iA12p14343>

881 Hamrin M, Norqvist P, André M, Eriksson AI (2002) A statistical study of wave properties  
882 and electron density at 1700 km in the auroral region. *J Geophys Res* 107(A8):1204.  
883 <https://doi.org/10.1029/2001JA900144>

884 Hatch SM, Moretto T, Lynch KA, Laundal KM, Gjerloev JW, Lund EJ (2020a) The  
885 relationship between cusp region ion outflows and east-west magnetic field  
886 fluctuations at 4,000-km altitude. *J Geophys Res Space Phys* 125:e2019JA027454.  
887 <https://doi.org/10.1029/2019JA027454>

888 Hatch SM, Haaland S, Laundal KM, Moretto T, Yau A, Bjoland LM, Reistad JP, Ohma  
889 A, Oksavik K (2020b) Seasonal and hemispheric asymmetries of F region polar cap

890 plasma density: Swarm and CHAMP observations. *J Geophys Res Space Phys*  
891 125:e2020JA028084. <https://doi.org/10.1029/2020JA028084>

892 Horwitz JL, Zeng W (2009) Physics-based formula representations of high-latitude  
893 ionospheric outflows: H<sup>+</sup> and O<sup>+</sup> densities, flow velocities and temperature vs. soft  
894 electron precipitation, wave-driven transverse heating, and solar zenith angle effects.  
895 *J Geophys Res* 114:A01308. <https://doi.org/10.1029/2008JA013595>

896 Huddleston MM, Chappell CR, Delcourt DC, Moore TE, Giles BL, Chandler MO (2005)  
897 An examination of the process and magnitude of ionospheric plasma supply to the  
898 magnetosphere. *J Geophys Res* 110:A12202. <https://doi.org/10.1029/2004JA010401>

899 Ilie R, Liemohn MW, Toth G, Ganushkina NY, Daldorff LKS (2015) Assessing the role  
900 of oxygen on ring current formation and evolution through numerical experiments. *J*  
901 *Geophys Res Space Phys* 120:4656–4668. <https://doi.org/10.1002/2015JA021157>

902 Ji EY, Jee G, Lee C (2019) Characteristics of the occurrence of ion upflow in association  
903 with ion/electron heating in the polar ionosphere. *J Geophys Res Space Phys*  
904 124:6226–6236. <https://doi.org/10.1029/2019JA026799>

905 Karimabadi H, Roytershteyn V, Mouikis CG, Kistler LM, Daughton W (2011) Flushing

906 effect in reconnection: Effects of minority species of oxygen ions. Planet Space Sci  
907 59:526–536. <https://doi.org/10.1016/j.pss.2010.07.014>

908 Kasahara Y, Hosoda T, Mukai T, Watanabe S, Kimura I, Kojima H, Niitsu R (2001)  
909 ELF/VLF waves correlated with transversely accelerated ions in the auroral region  
910 observed by Akebono. J Geophys Res 106:21123–21136.  
911 <https://doi.org/10.1029/2000JA000318>

912 Keika K, Nose M, Brandt P, Ohtani S, Mitchell DG, Roelof EC (2006) Contribution of  
913 charge exchange loss to the storm time ring current decay: IMAGE/HENA  
914 observations. J Geophys Res 111:A11S12. <https://doi.org/10.1029/2006JA011789>

915 Keika K, Kistler LM, Brandt PC (2013) Energization of O<sup>+</sup> ions in the Earth's inner  
916 magnetosphere and the effects on ring current buildup: A review of previous  
917 observations and possible mechanisms. J Geophys Res Space Phys 118:4441–4464.  
918 <https://doi.org/10.1002/jgra.50371>

919 Keika K, Seki K, Nosé M, Miyoshi Y, Lanzerotti LJ, Mitchell DG, Gkioulidou M,  
920 Manweiler JW (2018a) Three-step buildup of the 17 March 2015 storm ring current:  
921 Implication for the cause of the unexpected storm intensification. J Geophys Res

922 Space Phys 123:414–428. <https://doi.org/10.1002/2017JA024462>

923 Keika K, Kasahara S, Yokota S, Hoshino M, Seki K, Nosé M, Amano T, Miyoshi Y,  
924 Shinohara I (2018b) Ion energies dominating energy density in the inner  
925 magnetosphere: Spatial distributions and composition, observed by Arase/MEP-i.  
926 Geophys Res Lett 45:12153–12162. <https://doi.org/10.1029/2018GL080047>

927 Kistler LM, Mouikis CG (2016) The inner magnetosphere ion composition and local time  
928 distribution over a solar cycle. J Geophys Res Space Phys 121(3):2009–2032.  
929 <https://doi.org/10.1002/2015JA021883>

930 Kistler LM, Galvin AB, Popecki MA, Simunac KDC, Farrugia C, Moebius E, Lee MA,  
931 Blush LM, Bochsler P, Wurz P, Klecker B, Wimmer-Schweingruber RF, Opitz A,  
932 Sauvaud JA, Thompson B, Russell CT (2010) Escape of O<sup>+</sup> through the distant tail  
933 plasma sheet. Geophys Res Lett 37:L21101. <https://doi.org/10.1029/2010GL045075>

934 Kistler LM, Mouikis CG, Asamura K, Yokota S, Kasahara S, Miyoshi Y, Keika K,  
935 Matsuoka A, Shinohara I, Hori T, Kitamura N, Petrinec SM, Cohen IJ, Delcourt DC  
936 (2019) Cusp and nightside auroral sources of O<sup>+</sup> in the plasma sheet. J Geophys Res  
937 Space Phys 124:10036–10047. <https://doi.org/10.1029/2019JA027061>

938 Kitamura N, Shinbori A, Nishimura Y, Ono T, Iizima M, Kumamoto A (2009) Seasonal  
939 variations of the electron density distribution in the polar region during  
940 geomagnetically quiet periods near solar maximum. J Geophys Res 114:A01206.  
941 <https://doi.org/10.1029/2008JA013288>

942 Kitamura N, Nishimura Y, Ono T, Kumamoto A, Shinbori A, Iizima M, Matsuoka A,  
943 Hairston MR (2010a) Temporal variations and spatial extent of the electron density  
944 enhancements in the polar magnetosphere during geomagnetic storms. J Geophys Res  
945 115:A00J02. <https://doi.org/10.1029/2009JA014499>

946 Kitamura N, Nishimura Y, Ono T, Ebihara Y, Terada N, Shinbori A, Kumamoto A, Abe T,  
947 Yamada M, Watanabe S, Matsuoka A, Yau AW (2010b) Observations of very-low-  
948 energy (<10 eV) ion outflows dominated by O<sup>+</sup> ions in the region of enhanced electron  
949 density in the polar cap magnetosphere during geomagnetic storms. J Geophys Res  
950 115:A00J06. <https://doi.org/10.1029/2010JA015601>

951 Kitamura N, Ogawa Y, Nishimura Y, Terada N, Ono T, Shinbori A, Kumamoto A, Truhlik  
952 V, Smilauer J (2011) Solar zenith angle dependence of plasma density and  
953 temperature in the polar cap ionosphere and low-altitude magnetosphere during

954 geomagnetically quiet periods at solar maximum. *J Geophys Res* 116:A08227.  
955 <https://doi.org/10.1029/2011JA016631>

956 Kitamura N, Seki K, Nishimura Y, Terada N, Ono T, Hori T, Strangeway RJ (2012)  
957 Photoelectron flows in the polar wind during geomagnetically quiet periods. *J*  
958 *Geophys Res* 117:A07214. <https://doi.org/10.1029/2011JA017459>

959 Kitamura N, Seki K, Nishimura Y, McFadden JP (2015) Limited impact of escaping  
960 photoelectrons on the terrestrial polar wind flux in the polar cap. *Geophys Res Lett*  
961 42, 3106–3113. <https://doi.org/10.1002/2015GL063452>

962 Kitamura N, Seki K, Nishimura Y, Abe T, Yamada M, Watanabe S, Kumamoto A,  
963 Shinbori A, Yau AW (2016) Thermal and Low-energy Ion Outflows in and through  
964 the Polar Cap. In Chappell CR, Schunk RW, Banks PM, Burch JL, Thorne RM (eds)  
965 Magnetosphere-Ionosphere Coupling in the Solar System. Geophysical Monograph  
966 Series, vol 222, AGU, Washington, D. C., pp 91–100.  
967 <https://doi.org/10.1002/9781119066880.ch7>

968 Klumpar DM (1979) Transversely accelerated ions: an ionospheric source of hot  
969 magnetospheric ions. *J Geophys Res* 84:4229–4237.

970 <https://doi.org/10.1029/JA084iA08p04229>

971 Klumpar DM, Möbius E, Kistler LM, Popecki M, Hertzberg E, Crocker K, Granoff M,  
972 Tang L, Carlson CW, McFadden J, Klecker B, Eberl F, Künne E, Kästle H, Ertl M,  
973 Peterson WK, Shelly EG, Hovestadt D (2001) The time-of-flight energy, angle, mass  
974 spectrograph (TEAMS) experiment for FAST. *Space Sci Rev* 98:197–219.  
975 [https://doi.org/10.1007/978-94-010-0332-2\\_8](https://doi.org/10.1007/978-94-010-0332-2_8)

976 Kronberg EA, Haaland SE, Daly PW, Grigorenko EE, Kistler LM, Fränz M, Dandouras  
977 I (2012) Oxygen and hydrogen ion abundance in the near-Earth magnetosphere:  
978 Statistical results on the response to the geomagnetic and solar wind activity  
979 conditions. *J Geophys Res* 117:A12208. <https://doi.org/10.1029/2012JA018071>

980 Kronberg EA, Ashour-Abdalla M, Dandouras I, Delcourt DC, Grigorenko EE, Kistler LM,  
981 Kuzichev IV, Liao J, Maggiolo R, Malova HV, Orlova KG, Perroomian V, Shklyar DR,  
982 Shprits YY, Welling DT, Zelenyi LM (2014) Circulation of heavy ions and their  
983 dynamical effects in the magnetosphere: recent observations and models. *Space Sci*  
984 *Rev* 184:173–235. <https://doi.org/10.1007/s11214-014-0104-0>

985 Kronberg EA, Grigorenko EE, Haaland SE, Daly PW, Delcourt DC, Luo H, Kistler LM,

986 Dandouras I (2015) Distribution of energetic oxygen and hydrogen in the near-Earth  
987 plasma sheet. *J Geophys Res Space Phys* 120:3415–3431.  
988 <https://doi.org/10.1002/2014JA020882>

989 Liu H, Ma SY, Schlegel K (2001) Diurnal, seasonal, and geomagnetic variations of large  
990 field-aligned ion upflows in the high-latitude ionospheric F region. *J Geophys Res*  
991 106:24651–24661. <https://doi.org/10.1029/2001JA900047>

992 Liu YH, Mouikis CG, Kistler LM, Wang S, Roytershteyn V, Karimabadi H (2015) The  
993 heavy ion diffusion region in magnetic reconnection in the Earth's magnetotail. *J*  
994 *Geophys Res Space Phys* 120:3535–3551. <https://doi.org/10.1002/2015JA020982>

995 Ma YZ, Zhang QH, Xing ZY, Jayachandran PT, Moen J, Heelis RA, Wang Y (2018)  
996 Combined contribution of solar illumination, solar activity, and convection to ion  
997 upflow above the polar cap. *J Geophys Res Space Phys* 123:4317–4328.  
998 <https://doi.org/10.1029/2017JA024974>

999 Maes L, Maggiolo R, De Keyser J, Dandouras I, Fear RC, Fontaine D, Haaland S (2015)  
1000 Solar illumination control of ionospheric outflow above polar cap arcs. *Geophys Res*  
1001 *Lett* 42(5):1304–1311. <https://doi.org/10.1002/2014GL062972>

1002 Maggiolo R, Kistler LM (2014) Spatial variation in the plasma sheet composition:  
1003 dependence on geomagnetic and solar activity. *J Geophys Res Space Phys* 119:2836–  
1004 2857. <https://doi.org/10.1002/2013JA019517>

1005 Meng CI (1982) Latitudinal variation of the polar cusp during a geomagnetic storm.  
1006 *Geophys Res Lett* 9:60–63. <https://doi.org/10.1029/GL009i001p00060>

1007 Meng CI (1983) Case studies of the storm time variation of the polar cusp. *J Geophys*  
1008 *Res* 88:137–149. <https://doi.org/10.1029/JA088iA01p00137>

1009 Menz AM, Kistler LM, Mouikis CG, Spence HE, Henderson MG (2019) Effects of a  
1010 realistic O<sup>+</sup> source on modeling the ring current. *J Geophys Res Space Phys*,  
1011 124:9953–9962. <https://doi.org/10.1029/2019JA026859>

1012 Mitani K, Seki K, Keika K, Gkioulidou M, Lanzerotti LJ, Mitchell DG, Kletzing CA,  
1013 Yoshikawa A, Obana Y (2019) Statistical study of selective oxygen increase in high-  
1014 energy ring current ions during magnetic storms. *J Geophys Res Space Phys*  
1015 124:3193–3209. <https://doi.org/10.1029/2018JA026168>

1016 Miyake W, Mukai T, Kaya N (1993) On the evolution of ion conics along the field line  
1017 from EXOS D observations. *J Geophys Res* 98:11127–11134.

1018 <https://doi.org/10.1029/92JA00716>

1019 Moore TE, Fok MC, Delcourt DC, Slinker SP, Fedder JA (2007) Global aspects of solar  
1020 wind–ionosphere interactions. *J Atmos Solar Terr Phys* 69:265–278.  
1021 <https://doi.org/10.1016/j.jastp.2006.08.009>

1022 Moore TE, Fok MC, Delcourt DC, Slinker SP, Fedder JA (2010) Global response to local  
1023 ionospheric mass ejection. *J Geophys Res* 115:A00J14.  
1024 <https://doi.org/10.1029/2010JA015640>

1025 Mouikis CG, Kistler LM, Liu YH, Klecker B, Korth A, Dandouras I (2010) H<sup>+</sup> and O<sup>+</sup>  
1026 content of the plasma sheet at 15–19 Re as a function of geomagnetic and solar activity.  
1027 *J Geophys Res* 115:A00J16. <https://doi.org/10.1029/2010JA015978>

1028 Mouikis CG, Bingham ST, Kistler LM, Farrugia CJ, Spence HE, Reeves GD, Gkioulidou  
1029 M, Mitchell DG, Kletzing CA (2019) The storm-time ring current response to ICMEs  
1030 and CIRs using Van Allen Probe Observations. *J Geophys Res Space Phys* 124:9017–  
1031 9039. <https://doi.org/10.1029/2019JA026695>

1032 Nilsson H, Waara M, Marghita O, Yamauchi M, Lundin R, Rème H, Sauvaud JA,  
1033 Dandouras I, Lucek E, Kistler LM, Klecker B, Carlson CW, Bavassano-Cattaneo MB,

1034 Korth A (2008) Transients in oxygen outflow above the polar cap as observed by the  
1035 Cluster spacecraft. *Ann Geophys* 26:3365–3373. [https://doi.org/10.5194/angeo-26-](https://doi.org/10.5194/angeo-26-3365-2008)  
1036 3365-2008

1037 Nosé M, Matsuoka A, Kumamoto A., et al. (2020) Oxygen torus and its coincidence with  
1038 EMIC wave in the deep inner magnetosphere: Van Allen Probe B and Arase  
1039 observations. *Earth Planets Space* 72:111. [https://doi.org/10.1186/s40623-020-](https://doi.org/10.1186/s40623-020-01235-w)  
1040 01235-w

1041 Norqvist P, André M, Tyrland M (1998) A statistical study of ion energization  
1042 mechanisms in the auroral region. *J Geophys Res* 103:23459–23473.  
1043 <https://doi.org/10.1029/98JA02076>

1044 Ohtani S, Nosé M, Christon SP, Lui ATY (2011) Energetic O<sup>+</sup> and H<sup>+</sup> ions in the plasma  
1045 sheet: Implications for the transport of ionospheric ions. *J Geophys Res* 116:A10211.  
1046 <https://doi.org/10.1029/2011JA016532>

1047 Omidi N, Bortnik J, Thorne R, Chen L (2013) Impact of cold O<sup>+</sup> ions on the generation  
1048 and evolution of EMIC waves. *J Geophys Res Space Phys* 118:434–445.  
1049 <https://doi.org/10.1029/2012JA018319>

1050 Ouellette JE, Brambles OJ, Lyon JG, Lotko W, Rogers BN (2013) Properties of outflow-  
1051 driven sawtooth substorms. *J Geophys Res Space Phys* 118:3223–3232.  
1052 <https://doi.org/10.1002/jgra.50309>

1053 Peterson WK, Collin HL, Doherty MF, Bjorklund CM (1992) O<sup>+</sup> and He<sup>+</sup> restricted and  
1054 extended (BI-modal) ion conic distributions. *Geophys Res Lett* 19:1439–1442.  
1055 <https://doi.org/10.1029/92GL01613>

1056 Peterson WK, Collin HL, Yau AW, Lennartsson OW (2001) Polar/Toroidal Imaging  
1057 Mass-Angle Spectrograph observations of suprathermal ion outflow during solar  
1058 minimum conditions. *J Geophys Res* 106:6059–6066.  
1059 <https://doi.org/10.1029/2000JA003006>

1060 Perroomian V, El-Alaoui M, Brandt PC (2011) The ion population of the magnetotail  
1061 during the 17 April 2002 magnetic storm: Large-scale kinetic simulations and  
1062 IMAGE/HENA observations. *J Geophys Res* 116:A05214.  
1063 <https://doi.org/10.1029/2010JA016253>

1064 Peterson WK, Collin HL, Lennartsson OW, Yau AW (2006) Quiet time solar illumination  
1065 effects on the fluxes and characteristic energies of ionospheric outflow. *J Geophys*

1066 Res 111:A11S05. <https://doi.org/10.1029/2005JA011596>

1067 Pham KH, Lotko W, Varney RH, Zhang B, & Liu J (2021) Thermospheric impact on the  
1068 magnetosphere through ionospheric outflow. *Journal of Geophys Res Space Phys*  
1069 126:e2020JA028656. <https://doi.org/10.1029/2020JA028656>

1070 Ren J, Zou S, Lu J, Giertych N, Chen Y, Varney RH, Reimer AS (2020) Statistical study  
1071 of ion upflow and downflow observed by PFISR. *J Geophys Res Space Phys*  
1072 125:e2020JA028179. <https://doi.org/10.1029/2020JA028179>

1073 Saito H, Yoshino T, Sato N (1987) Narrow-banded ELF emissions over the southern polar  
1074 region. *Planet Space Sci* 35:745–752. [https://doi.org/10.1016/0032-0633\(87\)90034-1](https://doi.org/10.1016/0032-0633(87)90034-1)

1075 Seki K, Hirahara M, Terasawa T, Mukai T, Saito Y, Machida S, Yamamoto T, Kokubun S  
1076 (1998) Statistical properties and possible supply mechanisms of tailward cold O<sup>+</sup>  
1077 beams in the lobe/mantle regions. *J Geophys Res* 103:4477–4489.  
1078 <https://doi.org/10.1029/97JA02137>

1079 Schunk RW, Sojka JJ (1997) Global ionosphere-polar wind system during changing  
1080 magnetic activity. *J Geophys Res* 102:11,625–11,651.  
1081 <https://doi.org/10.1029/97JA00292>

1082 Schillings A, Nilsson H, Slapak R, Yamauchi M, Westerberg L-G (2017) Relative  
1083 outflow enhancements during major geomagnetic storms—Cluster observations. *Ann*  
1084 *Geophys* 35(6):1341–1352. <https://doi.org/10.5194/angeo-35-1341-2017>

1085 Schillings A, Nilsson H, Slapak R, Wintoft P, Yamauchi M, Wik M, Dandouras I, Carr  
1086 CM (2018) O<sup>+</sup> escape during the extreme space weather event of 4–10 September  
1087 2017. *Space Weather* 16(9):1363–1376. <https://doi.org/10.1029/2018SW001881>

1088 Schillings A, Slapak R, Nilsson H, Yamauchi M, Dandouras I, Westerberg LG (2019)  
1089 Earth atmospheric loss through the plasma mantle and its dependence on solar wind  
1090 parameters. *Earth Planets Space* 71:70. <https://doi.org/10.1186/s40623-019-1048-0>.

1091 Schillings A, Gunell H, Nilsson H, De Spiegeleer A, Ebihara Y, Westerberg LG,  
1092 Yamauchi M, Slapak R (2020) The fate of O<sup>+</sup> ions observed in the plasma mantle:  
1093 particle tracing modelling and cluster observations. *Ann Geophys* 38:645–656.  
1094 <https://doi.org/10.5194/angeo-38-645-2020>

1095 Slapak R, Schillings A, Nilsson H, Yamauchi M, Westerberg L-G, Dandouras I (2017)  
1096 Atmospheric loss from the dayside open polar region and its dependence on  
1097 geomagnetic activity: implications for atmospheric escape on evolutionary timescales.

1098 Ann Geophys 35:721–731. <https://doi.org/10.5194/angeo-35-721-2017>

1099 Shay MA, Swisdak M (2004) Three-species collisionless reconnection: Effect of O<sup>+</sup> on  
1100 magnetotail reconnection. Phys Rev Lett 93:175,001.  
1101 <https://doi.org/10.1103/PhysRevLett.93.175001>

1102 Strangeway RJ, Ergun RE, Su YJ, Carlson CW, Elphic RC (2005) Factors controlling  
1103 ionospheric outflows as observed at intermediate altitudes. J Geophys Res  
1104 110:A03221. <https://doi.org/10.1029/2004JA010829>

1105 Su YJ, Caton RG, Horwitz JL, Richards PG (1999) Systematic modeling of soft-electron  
1106 precipitation effects on high-latitude *F* region and top side ionospheric upflows. J  
1107 Geophys Res 104:153–163. <https://doi.org/10.1029/1998JA900068>

1108 Tenfjord P, Hesse M, Norgren C, Spinnangr SF, Kolstø H (2019) The impact of oxygen  
1109 on the reconnection rate. Geophys Res Lett 46:6195–6203.  
1110 <https://doi.org/10.1029/2019GL082175>

1111 Tung YK, Carlson CW, McFadden JP, Klumpar DM, Parks GK, Peria WJ, Liou K (2001)  
1112 Auroral polar cap boundary ion conic outflow observed on FAST. J Geophys Res  
1113 106:3603–3614. <https://doi.org/10.1029/2000JA900115>

1114 Valek PW, Delmonico E, McComas DJ, Goldstein J, Allegrini F, Livi S (2018)  
1115 Composition of 1–128 keV magnetospheric ENAs. *J Geophys Res Space Phys*  
1116 123:2668–2678. <https://doi.org/10.1002/2017JA024997>

1117 Varney RH, Wiltberger M, Lotko W (2015) Modeling the interaction between convection  
1118 and nonthermal ion outflows. *J Geophys Res Space Phys* 120:2353–2362.  
1119 <https://doi.org/10.1002/2014JA020769>

1120 Varney R, Wiltberger M, Zhang B, Lotko W, Lyon J (2016) Influence of ion outflow in  
1121 coupled geospace simulations: 2. Sawtooth oscillations driven by physics-based ion  
1122 outflow. *J Geophys Res Space Phys* 121:9688–9700.  
1123 <https://doi.org/10.1002/2016JA022778>

1124 Welling DT, Jordanova VK, Zaharia SG, Glocer A, Toth G (2011) The effects of dynamic  
1125 ionospheric outflow on the ring current. *J Geophys Res* 116:A00J19.  
1126 <https://doi.org/10.1029/2010JA015642>

1127 Welling DT, Jordanova VK, Glocer A, Toth G, Liemohn MW, Weimer DR (2015) The  
1128 two-way relationship between ionospheric outflow and the ring current. *J Geophys*  
1129 *Res Space Phys* 120:4338–4353. <https://doi.org/10.1002/2015JA021231>

1130 Welling DT, André M, Dandouras I, Delcourt D, Fazakerley A, Fontaine D, Foster J, Ilie  
1131 R, Kistler L, Lee JH, Liemohn MW, Slavin JA, Wang CP, Wiltberger M, Yau A (2016)  
1132 The Earth: Plasma sources, losses, and transport processes. In Nagy A, Blanc M,  
1133 Chappell C, Krupp N (eds) Plasma Sources of Solar System Magnetospheres. Space  
1134 Sciences Series of ISSI, vol 52, Springer, New York, pp. 145–208.  
1135 [https://doi.org/10.1007/978-1-4939-3544-4\\_5](https://doi.org/10.1007/978-1-4939-3544-4_5)

1136 Welling DT, Barakat AR, Eccles JV, Schunk RW, Chappell CR (2016) Coupling the  
1137 Generalized Polar Wind Model to Global Magnetohydrodynamics. In Chappell CR,  
1138 Schunk RW, Banks PM, Burch JL, Thorne RM (eds) Magnetosphere-Ionosphere  
1139 Coupling in the Solar System. Geophysical Monograph Series, vol 222, AGU,  
1140 Washington, D. C., pp. 179–194. <https://doi.org/10.1002/9781119066880.ch14>

1141 Wilson GR, Ober DM, Germany GA, Lund EJ (2004) Nightside auroral zone and polar  
1142 cap ion outflow as a function of substorm size and phase. *J Geophys Res* 109:A02206.  
1143 <https://doi.org/10.1029/2003JA009835>

1144 Wiltberger M, Lotko W, Lyon JG, Daminao P, Merkin V (2010) Influence of cusp O<sup>+</sup>  
1145 outflow on magnetotail dynamics in a multifluid MHD model of the magnetosphere.

- 1146 J Geophys Res 115, A00J05. <https://doi.org/10.1029/2010JA015579>
- 1147 Yamauchi M (2019) Terrestrial ion escape and relevant circulation in space. *Ann Geophys*
- 1148 37(6):1197–1222. <https://doi.org/10.5194/angeo-37-1197-2019>
- 1149 Yao Y, Seki K, Miyoshi Y, McFadden JP, Lund EJ, Carlson CW (2008a) Effect of solar
- 1150 wind variation on low-energy O<sup>+</sup> populations in the magnetosphere during
- 1151 geomagnetic storms: FAST observations. *J Geophys Res* 113:A04220.
- 1152 <https://doi.org/10.1029/2007JA012681>
- 1153 Yao Y, Seki K, Miyoshi Y, McFadden JP, Lund EJ, Carlson CW (2008b) Statistical
- 1154 properties of the multiple ion band structures observed by the FAST satellite. *J*
- 1155 *Geophys Res* 113:A07204. <https://doi.org/10.1029/2008JA013178>
- 1156 Yau AW, Beckwith PH, Peterson WK, Shelley EG (1985) Long-term (solar cycle) and
- 1157 seasonal variations of upflowing ionospheric ion events at DE 1 altitudes. *J Geophys*
- 1158 *Res* 90:6395–6407. <https://doi.org/10.1029/JA090iA07p06395>
- 1159 Yau AW, Abe T, Peterson WK (2007) The polar wind: recent observations. *J Atmos Solar*
- 1160 *Terr Phys* 69(16):1936–1983. <https://doi.org/10.1016/j.jastp.2007.08.010>
- 1161 Yu Y, Ridley AJ (2013) Exploring the influence of ionospheric O<sup>+</sup> outflow on

- 1162 magnetospheric dynamics: dependence on the source location. *J Geophys Res Space*
- 1163 *Phys* 118:1711–1722. <https://doi.org/10.1029/2012JA018411>
- 1164 Zeng C, Wang C, Duan S, Dai L, Fuselier SA, Burch JL, Torbert RB, Giles BL (2020)
- 1165 Statistical study of oxygen ions abundance and spatial distribution in the dayside
- 1166 magnetopause boundary layer: MMS observations. *J Geophys Res Space Phys*
- 1167 125:e2019JA027323. <https://doi.org/10.1029/2019JA027323>
- 1168 Zhang SR, Holt JM, van Eyken AP, Heinselman C, McCready M (2010) IPY
- 1169 observations of ionospheric yearly variations from high- to middle-latitude incoherent
- 1170 scatter radars. *J Geophys Res* 115:A03303. <https://doi.org/10.1029/2009JA014327>
- 1171 Zhang B, Brambles OJ, Lotko W, Lyon JG (2020) Is nightside outflow required to induce
- 1172 magnetospheric sawtooth oscillations. *Geophys Res Lett* 47:e2019GL086419.
- 1173 <https://doi.org/10.1029/2019GL086419>
- 1174 Zheng Y, Moore TE, Mozer FS, Russell CT, Strangeway RJ (2005) Polar study of
- 1175 ionospheric ion outflow versus energy input. *J Geophys Res* 110:A07210.
- 1176 <https://doi.org/10.1029/2004JA010995>
- 1177 Zhao K, Kistler LM, Lund EJ, Nowrouzi N, Kitamura N, Strangeway, RJ (2020) Factors

1178 controlling  $O^+$  and  $H^+$  outflow in the cusp during a geomagnetic storm:  
1179 FAST/TEAMS observations. Geophys Res Lett 46:e2020GL086975.  
1180 <https://doi.org/10.1029/2020GL086975>

1181 Zong QG, Fritz TA, Spence HE, Oksavik K, Pu ZY, Korth A, Daly PW (2004) Energetic  
1182 particle sounding of the magnetopause: A contribution by Cluster/RAPID. J Geophys  
1183 Res 109:A04207. <https://doi.org/10.1029/2003JA009929>

1184

## 1185 **Figure legends**

1186 **Figure 1.** Example of observations at high latitudes. Omnidirectional energy-time  
1187 spectrograms of differential energy flux of **a** electrons and **b** ions, and **c** number fluxes  
1188 of ions observed by IESA. Blue, black, red, and green bars indicate the periods of the  
1189 outflow regions, the subauroral zones, the double loss cones, and the polar cap,  
1190 respectively.

1191

1192 **Figure 2.** SZA distributions of averaged ion number flux in each event. Events at **a** all  
1193 MLT, **b** only around noon (0800–1600 MLT), and **c** only around midnight (2200–2400

1194 or 0000–0400 MLT). Different symbols and colors indicate different levels of the *Kp*  
1195 index.

1196

1197 **Figure 3.** Relations between the electron density in the loss cone (<50 eV) and the  
1198 mapped outflowing ion number flux in the SZA ranges of **a** 45°–85°, **b** 65°–105°, **c**  
1199 85°–125°, and **d** 105°–145°, and **f** comparisons among the derived empirical relations in  
1200 these SZA ranges and the empirical formula derived by Strangeway et al. (2005) (their  
1201 Equation 4) (multiplied by a factor of 2.9 to correct for the altitudinal difference of the  
1202 ion number flux) (dotted gray line). Weighted averages and standard deviations are  
1203 plotted as red crosses and solid lines. Dotted red lines indicate the empirical relations  
1204 derived by the fitting. In Figure 3e, the empirical relations in the SZA ranges of 45°–  
1205 85°, 65°–105°, 85°–125°, and 105°–145° are shown using red-dashed, orange dashed-  
1206 dotted-dotted, green dashed-dotted, and blue solid lines, respectively.

1207

1208 **Figure 4.** Relations between the precipitating electron density (<50 eV) and the  
1209 mapped outflowing ion number flux in the SZA ranges of **a** 45°–85°, **b** 65°–105°, **c**

1210 85°–125°, and **d** 105°–145°, and **e** comparisons among the derived empirical relations  
1211 in these SZA ranges and the empirical formula derived by Strangeway et al. (2005)  
1212 (their Equation 3) (multiplied by a factor of 2.9 to correct for the altitudinal difference  
1213 of the ion number flux and the precipitating electron density) (dotted gray line). The  
1214 format is identical to that of Figure 3. There are three data points below precipitating  
1215 electron density of  $3 \times 10^{-3} \text{ cm}^{-3}$ .

1216

1217 **Figure 5.** Relations between the mapped DC Poynting flux (<0.125 Hz) and the  
1218 mapped outflowing ion number flux in the SZA ranges of **a** 45°–85°, **b** 65°–105°, **c**  
1219 85°–125°, **d** 105°–145°, and **e** 45°–145° (all events), and **f** comparisons among the  
1220 derived empirical relations in these SZA ranges and the empirical formula derived by  
1221 Strangeway et al. (2005) (their Equation 5) (multiplied by a factor of 2.9 to correct for  
1222 the altitudinal difference of the ion number flux and the DC Poynting flux) (dotted gray  
1223 line). The format of Figure 5a–5e is identical to that of Figure 3a–3d. In Figure 5f, the  
1224 empirical relations in the SZA ranges of 45°–145° (all data) are shown using a thick  
1225 black line, in addition to the format of Figure 3e.

1226

1227 **Figure 6.** Relations between the mapped Alfvén Poynting flux (0.125–0.5 Hz) and the  
1228 mapped outflowing ion number flux in the SZA ranges of **a** 45°–85°, **b** 65°–105°, **c**  
1229 85°–125°, **d** 105°–145°, and **e** 45°–145° (all events), and **f** comparisons among the  
1230 derived empirical relations in the SZA ranges and the empirical formula derived by  
1231 Brambles et al. (2011) (multiplied by a factor of 2.9 here to correct for the altitudinal  
1232 difference of the ion number flux and the Alfvén Poynting flux) (dotted gray line). The  
1233 format is identical to that of Figure 5.

1234

# Figures

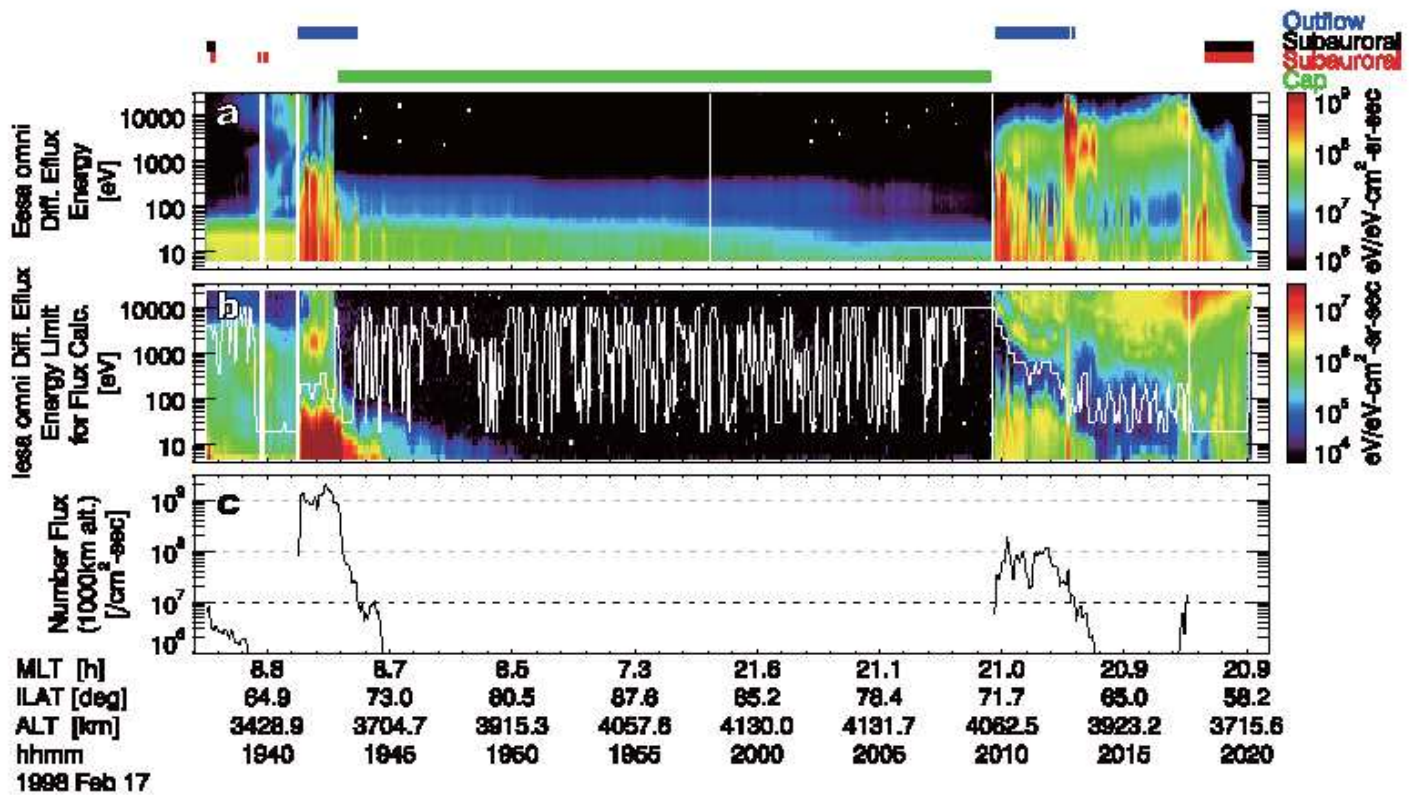
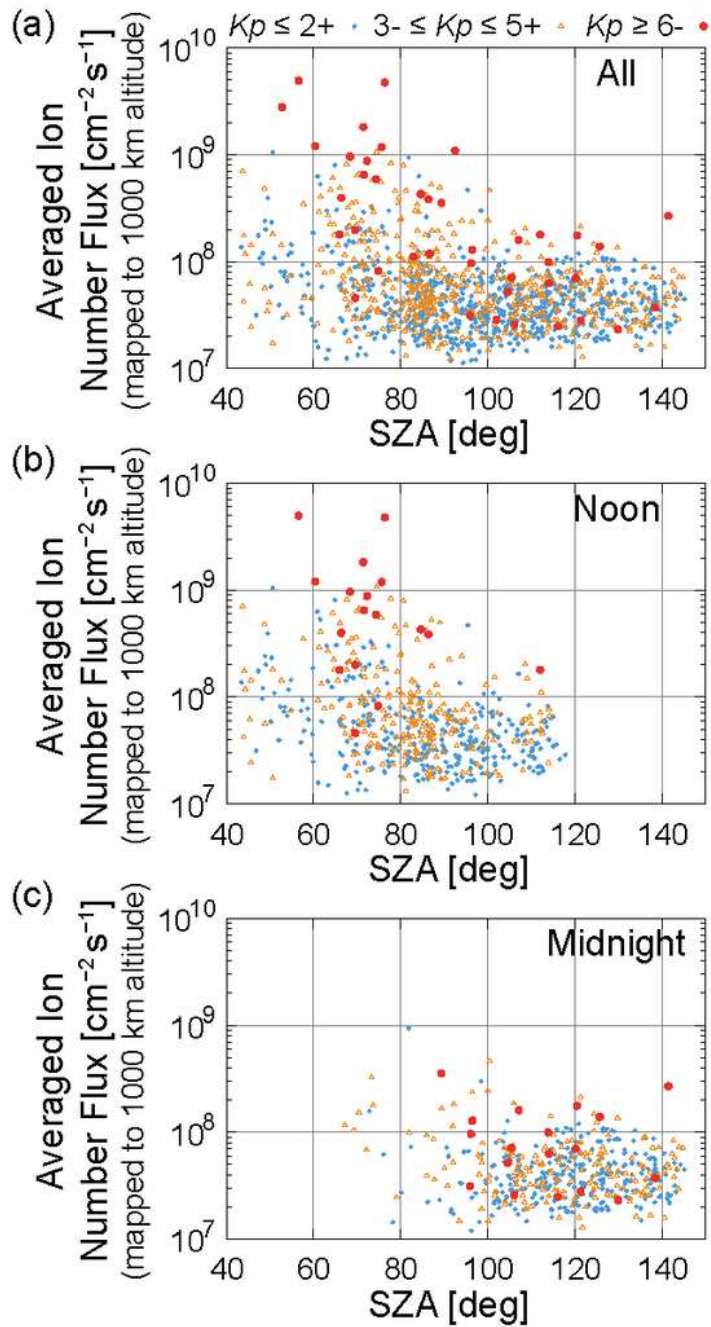


Figure 1

Example of observations at high latitudes. Omnidirectional energy-time spectrograms of differential energy flux of a electrons and b ions, and c number fluxes of ions observed by IESA. Blue, black, red, and green bars indicate the periods of the outflow regions, the subauroral zones, the double loss cones, and the polar cap, respectively.



**Figure 2**

SZA distributions of averaged ion number flux in each event. Events at a all MLT, b only around noon (0800–1600 MLT), and c only around midnight (2200–2400 or 0000–0400 MLT). Different symbols and colors indicate different levels of the Kp index.

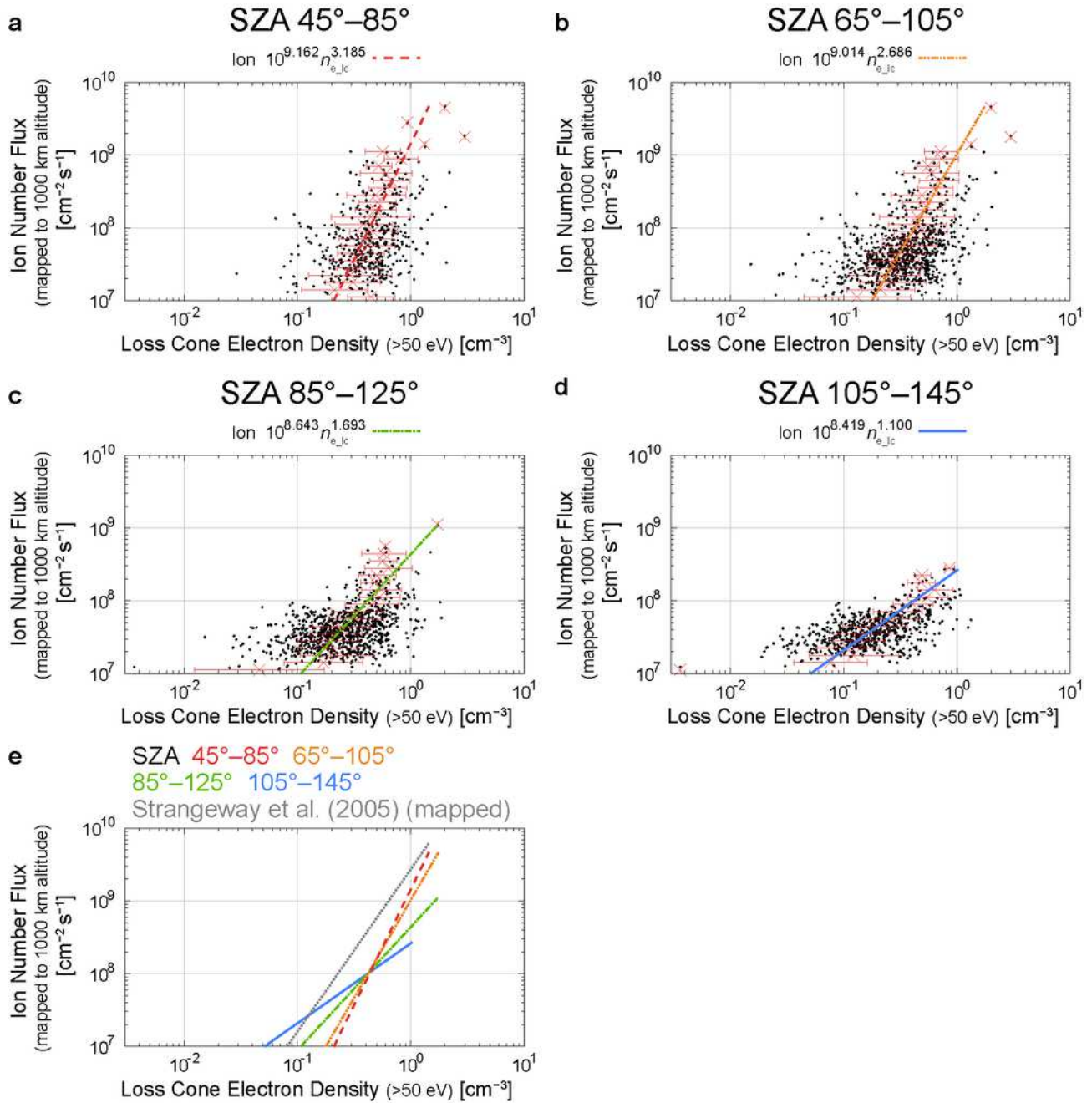


**Figure 3**

Relations between the electron density in the loss cone (<50 eV) and the mapped outflowing ion number flux in the SZA ranges of a 45°–85°, b 65°–105°, c 85°–125°, and d 105°–145°, and f comparisons among the derived empirical relations in these SZA ranges and the empirical formula derived by Strangeway et al. (2005) (their Equation 4) (multiplied by a factor of 2.9 to correct for the altitudinal difference of the ion number flux) (dotted gray line). Weighted averages and standard deviations are

plotted as red crosses and solid lines. Dotted red lines indicate the empirical relations derived by the fitting. In Figure 3e, the empirical relations in the SZA ranges of 45°–85°, 65°–105°, 85°–125°, and 105°–145° are shown using red-dashed, orange dashed-dotted-dotted, green dashed-dotted, and blue solid lines, respectively.

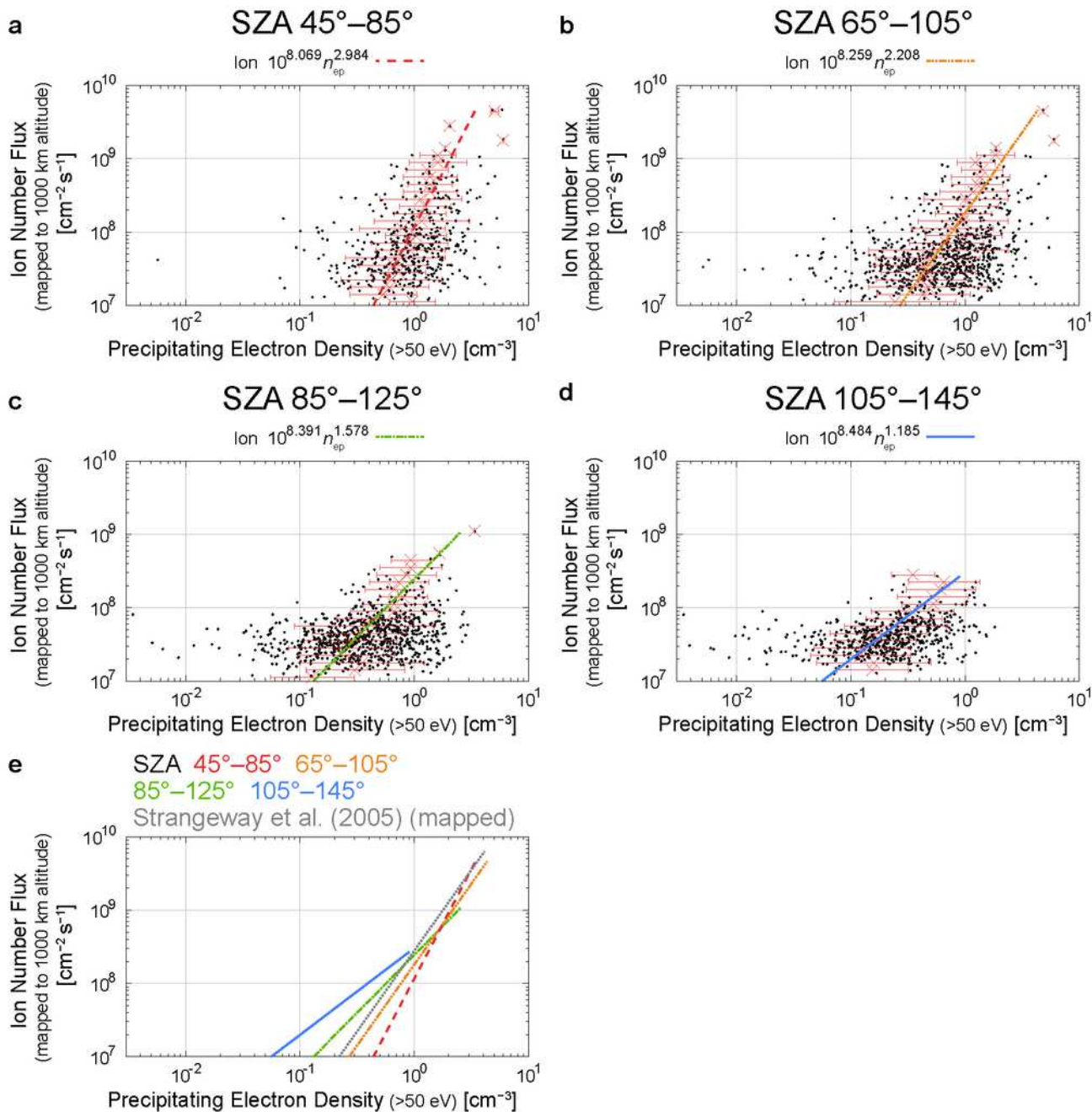


Figure 4

Relations between the precipitating electron density (<50 eV) and the mapped outflowing ion number flux in the SZA ranges of a 45°–85°, b 65°–105°, c 85°–125°, and d 105°–145°, and e comparisons among the derived empirical relations in these SZA ranges and the empirical formula derived by Strangeway et al. (2005) (their Equation 3) (multiplied by a factor of 2.9 to correct for the altitudinal difference of the ion number flux and the precipitating electron density) (dotted gray line). The format is identical to that of Figure 3. There are three data points below precipitating electron density of  $3 \times 10^{-3} \text{ cm}^{-3}$ .

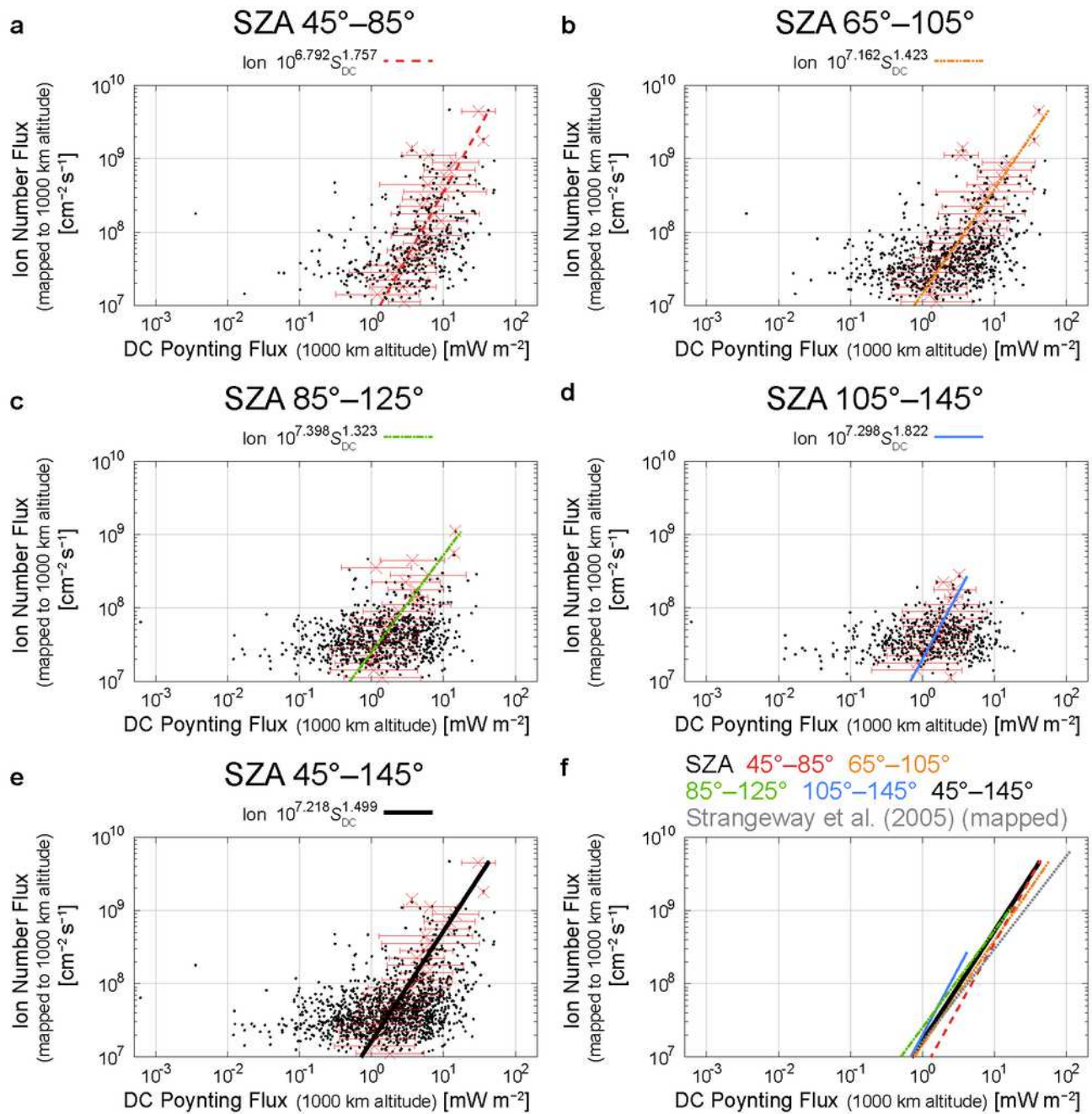
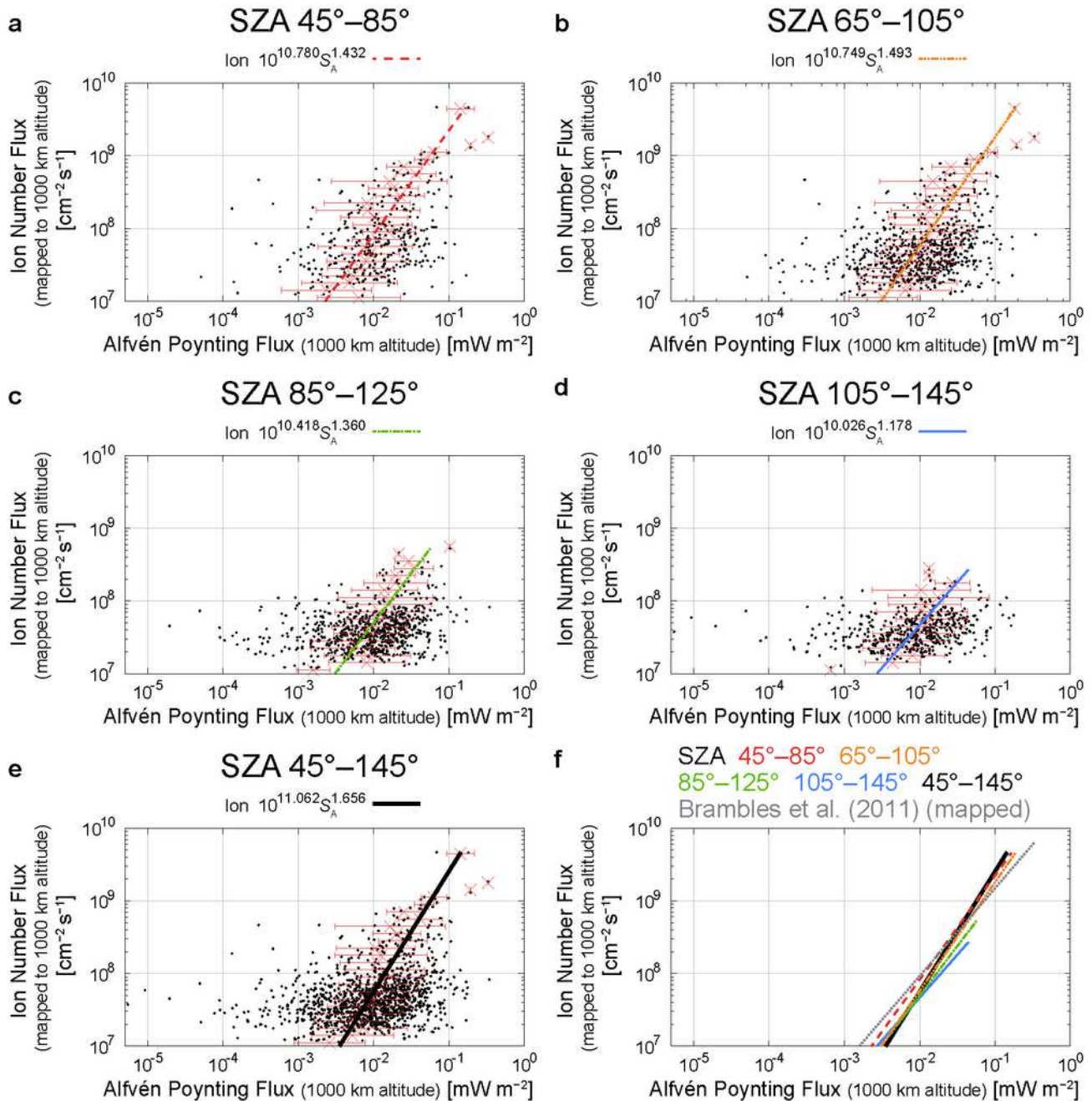


Figure 5

Relations between the mapped DC Poynting flux ( $<0.125$  Hz) and the mapped outflowing ion number flux in the SZA ranges of a  $45^\circ$ – $85^\circ$ , b  $65^\circ$ – $105^\circ$ , c  $85^\circ$ – $125^\circ$ , d  $105^\circ$ – $145^\circ$ , and e  $45^\circ$ – $145^\circ$  (all events), and f comparisons among the derived empirical relations in these SZA ranges and the empirical formula derived by Strangeway et al. (2005) (their Equation 5) (multiplied by a factor of 2.9 to correct for the altitudinal difference of the ion number flux and the DC Poynting flux) (dotted gray line). The format of Figure 5a–5e is identical to that of Figure 3a–3d. In Figure 5f, the empirical relations in the SZA ranges of  $45^\circ$ – $145^\circ$  (all data) are shown using a thick black line, in addition to the format of Figure 3e.



## Figure 6

Relations between the mapped Alfvén Poynting flux (0.125–0.5 Hz) and the mapped outflowing ion number flux in the SZA ranges of a 45°–85°, b 65°–105°, c 85°–125°, d 105°–145°, and e 45°–145° (all events), and f comparisons among the derived empirical relations in the SZA ranges and the empirical formula derived by Brambles et al. (2011) (multiplied by a factor of 2.9 here to correct for the altitudinal difference of the ion number flux and the Alfvén Poynting flux) (dotted gray line). The format is identical to that of Figure 5.

## Supplementary Files

This is a list of supplementary files associated with this preprint. Click to download.

- [GraphicalAbstract.png](#)